

Accelerating Analytic-Continuation GW Calculations with a Laplace Transformation and Natural Auxiliary Functions

Johannes Tölle,^{*,†,¶} Niklas Niemeyer,^{‡,¶} and Johannes Neugebauer^{*,‡}

[†]*Division of Chemistry and Chemical Engineering,
California Institute of Technology, Pasadena, California 91125, USA*

[‡]*University of Münster, Organisch-Chemisches Institut and
Center for Multiscale Theory and Computation,
Corrensstraße 36, 48149 Münster, Germany*

[¶]*Both authors contributed equally.*

E-mail: jtolle@caltech.edu; j.neugebauer@uni-muenster.de

Abstract

We present a simple and accurate GW implementation based on a combination of a Laplace transformation (LT) and other acceleration techniques used in post-SCF quantum chemistry, namely, natural auxiliary functions and the frozen-core approximation. The LT-GW approach combines three major benefits: (a) a small prefactor for the computational scaling, (b) easy integration into existing molecular GW implementations, and (c) significant performance improvements for a wide range of possible applications. Illustrating these advantages for systems consisting of up to 352 atoms and 7412 basis functions, we further demonstrate the benefits of this approach combined with an efficient implementation of the Bethe–Salpeter equation.

1 Introduction

After its introduction in 1965,¹ the GW (G: time ordered one-body Green’s function, W: screened Coulomb interaction) method has now become the standard approach for the accurate *ab-initio* determination of ionization potentials (IPs), electron affinities (EAs) (or more generally quasi-particle energies), and in combination with the Bethe–Salpeter equation (BSE), for excitation energies in condensed matter physics.^{2–8} The adoption within the realm of quantum chemistry has been established in recent years^{9–19} with the availability of implementations in a wide range of molecular quantum chemistry codes, see e.g., Refs. 9,12,16,20–30. The success of the GW method is owed to the fact that it offers good accuracy while being computationally feasible for a wide range of systems, c.f. Ref. 31. However, the GW method generally relies on error cancellation, and G_0W_0 , in particular, depends on the starting point chosen, the approach used for determining the dielectric function, and the self-consistency scheme chosen for the GW calculation. An excellent overview of the different aspects related to the GW approximation can be found in Ref. 32.

Especially the computational cost for determining the screened Coulomb interaction and therefore the G_0W_0 self-energy Σ_0 varies significantly for different practical realizations of the GW method in molecular orbital bases. The “fully-analytic” approach,^{33,34} for example, scales as $\mathcal{O}(N^6)$. The scaling can be reduced significantly by numerical integration of the self-energy Σ_0 ,

$$\Sigma_0(\mathbf{r}, \mathbf{r}', \omega) = \frac{i}{2\pi} \int d\omega' e^{i\omega'\eta} G_0(\mathbf{r}, \mathbf{r}', \omega + \omega') W_0(\mathbf{r}, \mathbf{r}', \omega'), \quad (1)$$

where the non-interacting one-particle Green’s function is denoted as G_0 and the screened Coulomb interaction as W_0 .

To avoid divergences along the real frequency axis,¹⁵ the integration in Eq. (1) is commonly performed along the imaginary frequency axis in combination with analytic continuation (AC) to the real frequency axis leading to a formal scaling of $\mathcal{O}(N^4)$.^{13,22,35} Alternatively,

one can employ the so-called contour-deformation approach (CD)^{15,22,36,37} by dividing the integration in Eq. (1) into an integration along the imaginary frequency axis and the real-frequency axis. The scaling, however, is $\mathcal{O}(N^{4-5})$ and depends on the quasi-particles to be determined (see Ref. 15).

Σ_0 can also be determined within the space-time formulation of the GW method.^{35,38-42} In this approach, the construction of W_0 is performed in imaginary-time rather than frequency space in combination with additional techniques, among others, real-space grid representation of the Green's function,^{39,43} pair atomic density fitting,¹⁷ or separable density-fitting^{42,44} to reduce the overall scaling to $\mathcal{O}(N^3)$ which allows for its application to systems containing almost 1000 atoms, e.g. Ref. 40. Note that this ansatz is equivalent to Laplace-transform (LT) techniques used in molecular quantum chemistry.⁴⁵⁻⁴⁷ Drawbacks of these methods are, however, related to increasing memory requirements and larger prefactors due to the real-space representation,³⁹ the careful error evaluation necessary concerning the various numerical procedures and chosen cut-offs,^{17,40} or the necessity to construct specialized real-space grids.⁴² These aspects also lead to more challenging numerical implementations of these methods, potentially limiting their widespread application. Note, however, that in the limit of very large systems, these approaches can be more beneficial compared to the methodology presented here.

This work demonstrates an alternative efficient evaluation of the GW self-energy by combining different ideas for reducing the computational cost based on the AC-GW formulation. In particular, we make use of a Laplace transformation for the evaluation of W_0 , a truncation of the auxiliary basis using natural auxiliary functions (NAF)^{48,49} and the frozen-core (FC) approximation. We refer to this approach as LT-GW in the following which is based on three guiding principles: (a) a small prefactor should be preserved, (b) adaptation of existing AC-GW implementations should require minimal effort, and (c) significant performance improvements should result for a wide range of system sizes with controllable error.

2 Theory

In the following, a concise overview of the modified GW implementation based on the Laplace-transform (LT) technique is given. More detailed information regarding GW implementations based on imaginary frequency integration can be found in Refs. 15,22,37.

A diagonal element nm for the correlation part of the screened-Coulomb interaction W_{nm}^c in a molecular orbital basis for an imaginary frequency $i\omega$ is calculated as

$$W_{nm}^c(i\omega') = \sum_{PQ} R_{nm}^P \left\{ [1 - \mathbf{\Pi}(i\omega')]_{PQ}^{-1} - \delta_{PQ} \right\} R_{nm}^Q, \quad (2)$$

where molecular spin-orbital (ϕ) and auxiliary basis function (χ) indices are given in lowercase and uppercase letters, respectively. Furthermore, i, j, \dots refer to occupied, a, b, \dots to virtual, and n, m, \dots to arbitrary orbitals with eigenvalues ϵ . $\mathbf{\Pi}_{PQ}(i\omega')$ is evaluated as

$$\mathbf{\Pi}_{PQ}(i\omega') = -2 \sum_{ia} R_{ia}^P \frac{(\epsilon_a - \epsilon_i)}{\omega'^2 + (\epsilon_a - \epsilon_i)^2} R_{ia}^Q, \quad (3)$$

and the transformed three-center integrals R_{nm}^P are defined as

$$R_{nm}^Q = \sum_P (nm|P)[\mathbf{V}^{-1/2}]_{PQ}, \quad (4)$$

with

$$(nm|P) = \int d\mathbf{r} \int d\mathbf{r}' \frac{\phi_n(\mathbf{r})\phi_m(\mathbf{r})\chi_P(\mathbf{r}')}{|\mathbf{r} - \mathbf{r}'|}, \quad (5)$$

and

$$V_{PQ} = \int d\mathbf{r} \int d\mathbf{r}' \frac{\chi_P(\mathbf{r})\chi_Q(\mathbf{r}')}{|\mathbf{r} - \mathbf{r}'|}. \quad (6)$$

In AC-GW, the construction of $\mathbf{\Pi}_{PQ}(i\omega')$ is the most time-consuming step, formally scaling

as $\mathcal{O}(N_o N_v N_{\text{aux}}^2)$ for each imaginary frequency (N_o being the number of occupied orbitals, N_v the number of virtual orbitals, and N_{aux} the number of auxiliary functions). Finally, the correlation (dynamical) part of the G_0W_0 self-energy Σ^c is obtained (ϵ_F denotes the Fermi-level)

$$\Sigma_n^c(i\omega) = -\frac{1}{\pi} \sum_m \int_0^\infty d\omega' \frac{i\omega + \epsilon_F - \epsilon_m}{(i\omega + \epsilon_F - \epsilon_m)^2 + \omega'^2} W_{nm}(i\omega'), \quad (7)$$

which is integrated numerically using a modified Gauss–Legendre (GL) quadrature, see Refs. 9,22. We note that different integration choices for Eq. (7) are possible. In this work, however, we restrict ourselves to a modified GL quadrature since it presumably is the most common numerical integration scheme used in the analytic-continuation GW context. Quasi-particle energies are then determined by AC of Σ^c to the real frequency axis. For the AC to the real frequency axis, we use a N -point Padé approximation as described in the appendix of Ref. 50.

In this work, we make use of the LT for evaluating $\Pi_{PQ}(i\omega')$. In a first step, the denominator in Eq. (3) is rewritten as

$$\begin{aligned} \frac{1}{\omega'^2 + (\epsilon_a - \epsilon_i)^2} &= \int_0^\infty d\tau \exp(-(\omega'^2 + (\epsilon_a - \epsilon_i)^2) \tau) \\ &= \int_0^\infty d\tau \exp(-\omega'^2 \tau) \exp(-(\epsilon_a - \epsilon_i)^2 \tau). \end{aligned} \quad (8)$$

holding for $(\omega'^2 + (\epsilon_a - \epsilon_i)^2) > 0$ which is guaranteed to be true. Replacing the denominator with the integral in Eq. (8) allows to apply a numerical integration of the form

$$\begin{aligned} \frac{1}{\omega'^2 + (\epsilon_a - \epsilon_i)^2} &\approx -\sum_m^{N_{\text{LT}}} w_m \exp(-(\omega'^2 + (\epsilon_a - \epsilon_i)^2) x_m) \\ &= -\sum_m^{N_{\text{LT}}} w_m \exp(-\omega'^2 x_m) \exp(-(\epsilon_a - \epsilon_i)^2 x_m), \end{aligned} \quad (9)$$

where the N_{LT} quadrature points and their corresponding weights are denoted as x_m and w_m ,

respectively. Factorizing the exponential functions with frequencies and orbital-energy differences as their arguments through the LT allows evaluating their contributions to $\Pi_{PQ}(i\omega')$ separately as

$$\Pi_{PQ}(i\omega') \approx -2 \sum_m \underbrace{\sum_{ia} R_{ia}^P w_m (\epsilon_a - \epsilon_i) e^{-(\epsilon_a - \epsilon_i)^2 x_m} R_{ia}^Q e^{-\omega'^2 x_m}}_{M_{PQ}^m}. \quad (10)$$

In practice, M_{PQ}^m is calculated for each quadrature point, which requires $N_{\text{LT}} N_o N_v N_{\text{aux}}^2$ operations, followed by the outer loop over imaginary frequencies [see Eq. (2)] counting $N_{\text{LT}} N_{\text{aux}}^2 N_{i\omega}$ operations. In contrast, the evaluation of Eq. (3) for the determination of quasi-particle energies requires $N_{i\omega} N_o N_v N_{\text{aux}}^2$ operations. It becomes clear that the formal scaling remains unchanged with $\mathcal{O}(N^4)$ since neither $N_{i\omega}$ nor N_{LT} depends on the system size represented by N . A constant speed-up can, however, be expected using the LT technique as long as $N_{\text{LT}} < N_{i\omega}$ which is proportional to the ratio $N_{i\omega}/N_{\text{LT}}$.

The natural auxiliary function (NAF) approximation⁴⁸ reduces the size of the three-index integral tensor that commonly appears in post-SCF methodology making use of the resolution of the identity approximation. Its basis is given by a symmetric, positive definite matrix K that reads

$$K_{PQ} = \sum_{nm} R_{nm}^P R_{nm}^Q. \quad (11)$$

A rank reduction of the three-index integral list is achieved by first diagonalizing K to yield the NAFs labeled by \tilde{P} ,

$$\sum_Q K_{PQ} V_{Q,\tilde{P}} = V_{P\tilde{P}} \epsilon_{\tilde{P}}, \quad (12)$$

followed by setting up a transformation matrix $U_{P\tilde{P}}$ that only includes NAFs with corresponding eigenvalues above a certain threshold ϵ_{NAF} (assembled from the columns of $V_{P\tilde{P}}$).

Finally, the three-center integral tensor is transformed to the NAF space following

$$R_{nm}^{\tilde{P}} = \sum_P R_{nm}^P U_{P\tilde{P}}. \tag{13}$$

In the limit of U including *all* eigenvectors of K , Eq. (13) represents an orthogonal transformation. Our implementation omits the virtual–virtual part of the sum in Eq. (11) due to its unfavorable scaling with the system size. Closed-shell molecules are handled by including a factor of two in Eq. (11) to account for the single set of spatial orbitals. Determining the NAFs formally scales as $\mathcal{O}(N_o N_v N_{\text{aux}}^2)$. The theoretical speed-up of the NAF approximation in AC-GW calculations becomes apparent when inspecting Eqs. (3) and (8). The time-determining step includes an inner product of the three-index integral tensor contracting the occupied–virtual composite index ia . As a result, the expected speed-up scales quadratically with the quotient of the number of original auxiliary basis functions N_{aux} and the number of NAFs N_{NAF} , that is, $(N_{\text{aux}}/N_{\text{NAF}})^2$.

3 Computational Details

All calculations presented in this article were performed with a slightly modified version of the SERENITY program (1.5.2).^{23–25} All self-consistent field (SCF) procedures were stopped as soon as two of the following convergence criteria have been met: total energy threshold of $5 \cdot 10^{-8} E_h$, root-mean-square deviation of the density matrix threshold of $5 \cdot 10^{-8}$ a.u., as well as a threshold of $5 \cdot 10^{-7}$ a.u. for the commutator of the Fock and density matrix. DFT calculations employ default grids as implemented in SERENITY. All calculations employ def2-TZVP basis sets⁵¹ and the GW and BSE calculations additionally use the corresponding RIFIT (RI-C) basis set.⁵² Unless explicitly stated otherwise, the resolution of the identity approximation is applied to the Coulomb part of the Fock matrix in SCF calculations with the universal def2/JFIT basis set.⁵³ GW calculations were performed within the analytic-continuation (AC) approach, include the energetically lowest and highest five virtual and

occupied SCF orbitals, unless stated otherwise, and employ 128 integration points along the imaginary frequency axis that were obtained from a modified Gauss–Legendre (GL) quadrature. The Padé approximation is performed based on 70 imaginary frequencies obtained from a modified Gauss–Legendre grid.^{9,22} Bethe–Salpeter equation (BSE) calculations were carried out within the Tamm–Dancoff and static (to the dielectric function) approximations. Eigenvectors in the iterative solution of the BSE were converged to maximum residual norms of 10^{-5} and GW quasi-particle energies are used for the construction of the static dielectric function. Orbitals not included in the quasi-particle calculation are shifted based on the difference between the lowest and highest quasi-particle energy and the respective KS orbital eigenvalue.^{26,37} We used six quasi-particle iterations for the water cluster, discussed in Fig. 1 and 2, and otherwise, quasi-particle iterations are performed until the change in the HOMO/LUMO gap is below 10^{-6} E_h. For calculations related to the GW100 benchmark, the imaginary broadening factor η is set to 0.0 for comparison purposes, while it is set to $\eta = 0.001$ a.u. for the remaining calculations. Quadrature points and weights for the Laplace transformation were obtained with the `laplace-minimax` library.^{54,55} For this, the lower bound of the denominator was chosen to be the squared difference of the highest occupied molecular orbital (HOMO) eigenvalue and the lowest unoccupied molecular orbital (LUMO) eigenvalue summed with the square of the smallest frequency. The upper bound was chosen to be the square of the largest energy difference of the energetically lowest occupied and highest unoccupied molecular orbital eigenvalues. If this upper bound is below 10^4 a.u., we use 10^4 a.u. instead to ensure an accurate numerical integration for a wide energy window. As shown in this article, these bounds together with the chosen threshold $\epsilon_{\text{LT}} = 10^{-7}$ for the square root of the error function of the LT procedure lead to negligible errors in the quasi-particle energies (< 0.1 meV). We note that this threshold is far tighter than commonly used thresholds in, e.g., coupled-cluster applications, where 10^{-3} – 10^{-4} is a standard choice.⁵⁶ In summary, all thresholds for numerical integration (LT-/modified Gauss–Legendre-grid) as well as the number of frequencies for the Padé approximation in

the AC procedure are chosen very conservatively in order to keep the introduced error as small as possible. An analysis of the influence of the size of the LT and Gauss–Legendre grid on the accuracy and computational timings in the determination of QP energies are discussed in Sec. 4.1.2 for a system consisting of 100 water molecules. Within the frozen-core (FC) approximation, a tabulated number of the energetically lowest-lying SCF orbitals for each atom are frozen in all post-SCF treatments. These numbers were chosen following the defaults in the ORCA program (as listed in Ref. 57).

4 Results

4.1 Quasi-particle energies using $LT-G_0W_0$

4.1.1 GW100

In the following, we will demonstrate the robustness, scalability, and speed-up of combining AC- G_0W_0 with the LT, NAF, and FC techniques. First, its accuracy is determined for the GW100 benchmark set.⁵⁸ Reference orbitals were obtained using the Hartree–Fock approximation throughout. Effective core potentials are used for the heavy elements rubidium, silver, xenon, and iodine. All results are compared to reference quasi-particle (QP) energies based on the “fully-analytic” evaluation of the G_0W_0 self-energy without employing the RI approximation (also for the mean-field calculation).¹⁰ The resulting deviations for the HOMO/LUMO quasi-particle energies are displayed in Fig. 1. Statistical measures [mean absolute error (MAE), maximum absolute error (MXAE) and standard deviation (SD)] are given in Tab. 1. The quasi-particle energies for all methods are explicitly shown in Tab. S1 (HOMO) and Tab. S2 (LUMO) in the Supporting Information (SI).

From Fig. 1 it becomes clear that especially for the HOMO quasi-particle energies evaluated with analytic-continuation (AC) in combination with the frozen-core (FC) approximation, larger deviations up to -0.08 eV for the HOMO quasi-particle energies of, for

example, krypton, bromine and carbon tetrabromide are observed. These systems also show comparatively large errors for the LUMO quasi-particle energies of -0.07 eV and -0.02 eV, respectively. These errors transfer to the quasi-particle energies evaluated within the AC/FC/NAF approximation. Because these errors originate from the FC approximation, we investigated the deviations in the quasi-particle energies of these systems by reducing the number of frozen electrons from $18 e^-$ to $10 e^-$. The resulting quasi-particle deviations are

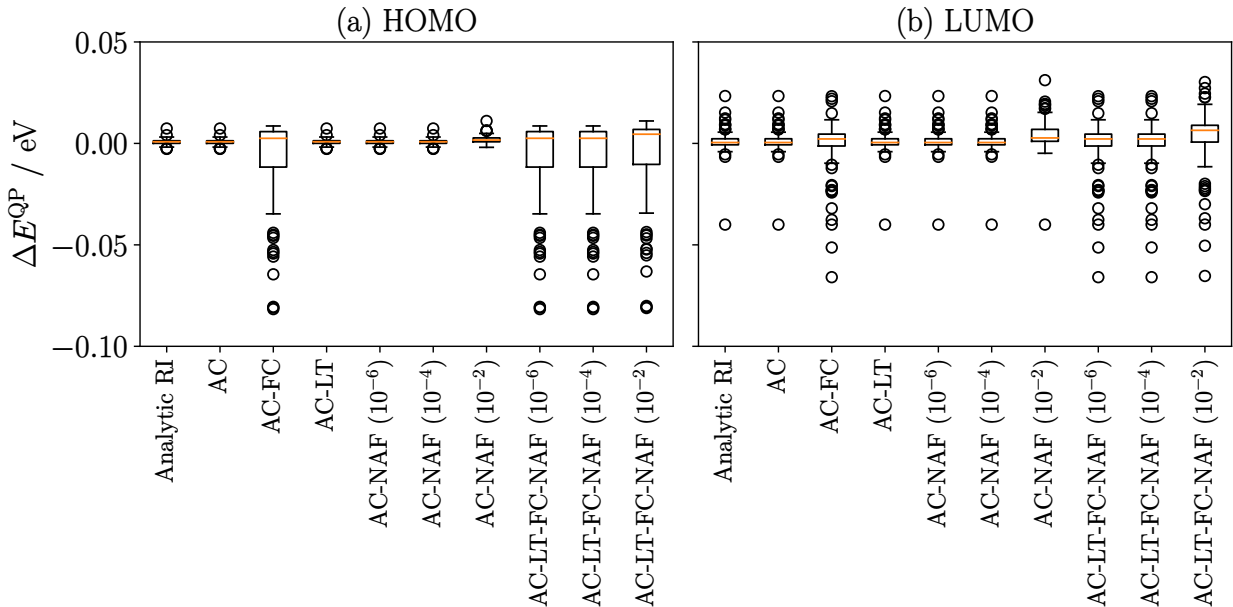


Figure 1: Deviations in the G_0W_0 (a) HOMO and (b) LUMO quasi-particle energies for the molecular systems from the GW100 benchmark set for various approximations in the evaluation of the G_0W_0 self-energy relative to the “fully-analytic” approach without employing the RI approximation. Analytic-RI: “Fully-analytic” approach using the RI approximation, AC: AC- G_0W_0 , LT: AC- G_0W_0 in combination with AC-LT ($\varepsilon_{LT} = 10^{-7}$), AC-FC: AC- G_0W_0 in combination with FC, AC-NAF: AC- G_0W_0 in combination with the NAF approximation ($\varepsilon_{NAF} = 10^{\{-6,-4,-2\}}$), AC-FC-LT-NAF: Combining AC- G_0W_0 with FC/LT/NAF ($\varepsilon_{LT} = 10^{-7}$, $\varepsilon_{NAF} = 10^{\{-6,-4,-2\}}$) [def2-TZVP, starting from Hartree–Fock orbitals]. The box plots were created with the `matplotlib.pyplot.boxplot` function of the `matplotlib` library using default settings. For each data set, the orange line marks the median, the top and bottom of the box mark the 25th and 75th percentiles, respectively, and their difference, i.e. the box height is the interquartile range (IQR). The lower and upper ends of the whiskers mark the lowest and highest value before the 25th percentile minus and 75th percentile plus, respectively, one and a half times the IQR. Circles mark values outside of this region, generally considered outliers. For further explanation of the different elements of the box plot, see Ref. 59. The HOMO and LUMO quasi-particle energies themselves are found in Tabs. S1 and S2.

Table 1: Mean absolute error (MAE), maximum absolute error (MXAE) and standard deviation (SD) in the G_0W_0 (a) HOMO and (b) LUMO quasi-particle energies for the molecular systems from the GW100 benchmark set for various approximations in the evaluation of the G_0W_0 self-energy relative to the “fully-analytic” approach without employing the RI approximation in meV. Analytic-RI: “Fully-analytic” approach using the RI approximation, AC: AC- G_0W_0 , LT: AC- G_0W_0 in combination with AC-LT ($\varepsilon_{LT} = 10^{-7}$), AC-FC: AC- G_0W_0 in combination with FC, AC-NAF: AC- G_0W_0 in combination with the NAF approximation ($\varepsilon_{NAF} = 10^{\{-6,-4,-2\}}$), AC-FC-LT-NAF: Combining AC- G_0W_0 with FC/LT/NAF ($\varepsilon_{LT} = 10^{-7}$, $\varepsilon_{NAF} = 10^{\{-6,-4,-2\}}$) [def2-TZVP, starting from Hartree-Fock orbitals].

	(a) HOMO			(b) LUMO		
	MAE	MXAE	SD	MAE	MXAE	SD
Analytic RI	1.1	7.3	1.4	2.9	40.0	5.8
AC	1.1	7.3	1.4	2.9	40.0	5.8
AC-FC	13.3	81.7	21.7	7.9	65.9	13.4
AC-LT	1.1	7.3	1.4	2.9	40.0	6.0
AC-NAF (10^{-6})	1.1	7.3	1.4	2.9	40.0	5.8
AC-NAF (10^{-4})	1.1	7.3	1.4	2.9	40.0	5.8
AC-NAF (10^{-2})	2.1	11.1	1.9	5.6	40.0	7.4
AC-LT-FC-NAF (10^{-6})	13.3	81.7	21.7	7.9	65.9	13.4
AC-LT-FC-NAF (10^{-4})	13.3	81.7	21.7	7.9	65.9	13.4
AC-LT-FC-NAF (10^{-2})	14.0	81.1	22.0	10.8	65.3	14.8

shown in Tab. 2. It can be seen that the errors with the modified FC are below 4 meV, which highlights that the FC can be systematically adjusted to reduce the resulting error in the quasi-particle energies. All systems studied beyond the GW100 benchmark set contain only first- and second-row elements (with WW-6 being an exception, which is, however, separately benchmarked against a regular AC- G_0W_0 calculation). For these systems, the FC approximation leads to only a small error. We, therefore, used the default number of frozen electrons in the remaining calculations. For the LUMO quasi-particle energies, we find that the deviation of the hydrogen system is much larger than for the rest of the systems already for the “Analytic RI” calculation (which transfers directly to all AC calculations, see the outlier in Fig. 1(b)). We can, therefore, conclude that these deviations are a result of the RI approximation for this system and that the LT, NAF, or FC approximations introduce only small and controllable errors. These deviations are much smaller than the intrinsic error of the G_0W_0 method itself, c.f. Ref. 31, justifying their application. Especially the loose NAF

Table 2: Deviations in the HOMO/LUMO G_0W_0 quasi-particle energies for AC- G_0W_0 in combination with the FC approximation (relative to the “fully-analytic” approach without employing the RI approximation), either freezing $18e^-$ or $10e^-$ of bromine, krypton, and carbon tetrabromide. The number of frozen carbon electrons remains unchanged [def2-TZVP, starting from Hartree–Fock orbitals].

Molecule	FC(18 e^-)		FC(10 e^-)	
	HOMO	LUMO	HOMO	LUMO
bromine	-0.0806	-0.0659	-0.0037	0.0034
krypton	-0.0809	-0.0230	-0.0020	0.0000
carbon tetrabromide	-0.0817	-0.0377	-0.0037	0.0010

threshold of 10^{-2} leads to almost negligible error. As a result, all further calculations shown in this article will be confined to this threshold.

4.1.2 Water clusters

Next, we performed G_0W_0 calculations on water clusters (see Fig. 3) of increasing size containing ten to 100 water molecules (corresponding to 430 to 4300 SCF basis functions in a def2-TZVP basis, respectively) and investigate QP energies and computational timings. The geometries were obtained by first generating a cubic $20 \times 20 \times 20 \text{ \AA}^3$ water cluster containing 233 water molecules with VMD,⁶⁰ optimizing it with GFN2-xTB (6.4.1)⁶¹ and then including the respective number of molecules closest to the center of mass of the whole cluster. In Fig. 2, we display the signed error in QP energies as a function of the number of molecules included in the water cluster for the HOMO and the LUMO for the different approximate strategies employed here as well as a combination thereof. Again, we find that the LT approximation does not introduce significant errors in QP energies for either the HOMOs or the LUMOs. For the NAF approximation ($\epsilon_{\text{NAF}} = 10^{-2}$), the error with respect to the reference calculation is constant at about 1.5 meV and 3.0 meV for the HOMO and the LUMO, respectively. For the FC approximation, a constant error of about 3.5 meV and -0.5 meV is observable for the HOMO and the LUMO energies, respectively. While the error of the approximation combining LT, NAF, and FC exceeds the individual errors in the

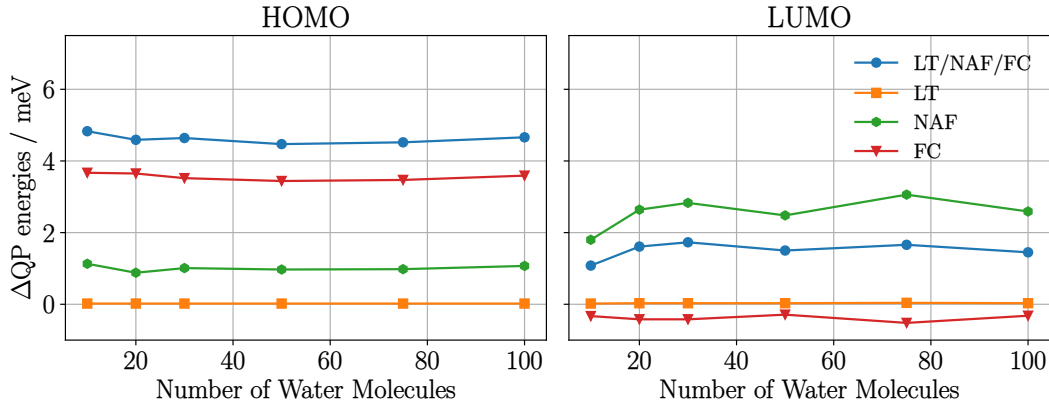


Figure 2: Signed error in the HOMO and LUMO G_0W_0 QP energies as a function of the number of molecules included in the water cluster shown in Fig. 3 [HF/def2-TZVP].

HOMO case (about 4.5 meV), we find partial error cancellation in the LUMO case (about 1.8 meV). Most importantly, however, it can be seen that (a) the error in QP energies is essentially independent of the system size and (b) the magnitude of QP energy errors is within a tolerable range using the approximations and thresholds suggested here (compare Sec. 3).

As a next step, we show computational timings of the various G_0W_0 methods. We assess the practical scaling behavior with the system size by considering linear fits of double logarithmic plots of the wall-clock timings for the calculation of the screened Coulomb interaction W_0 [see, e.g., Eq. (2)] as a function of the number of SCF basis functions in Fig. 3. A non-logarithmic wall-clock timing plot along with the resulting speed-ups can be found in Fig. S1 of the Supporting Information. It can be argued that considering the slopes of the linear fits could be considered unsuitable here, as the formal scaling of each variant of our LT-GW approach remains unchanged with $\mathcal{O}(N^4)$. As a result, no difference in slopes is to be expected between the approaches in the limit where the respective algorithmic step with the highest-order scaling behavior dominates the computation time. We add those fits mainly to estimate the practical scaling implications for typical system sizes in molecular quantum-chemistry applications.

Taking a look at the corresponding linear fits performed on the data in Fig. 3, we find

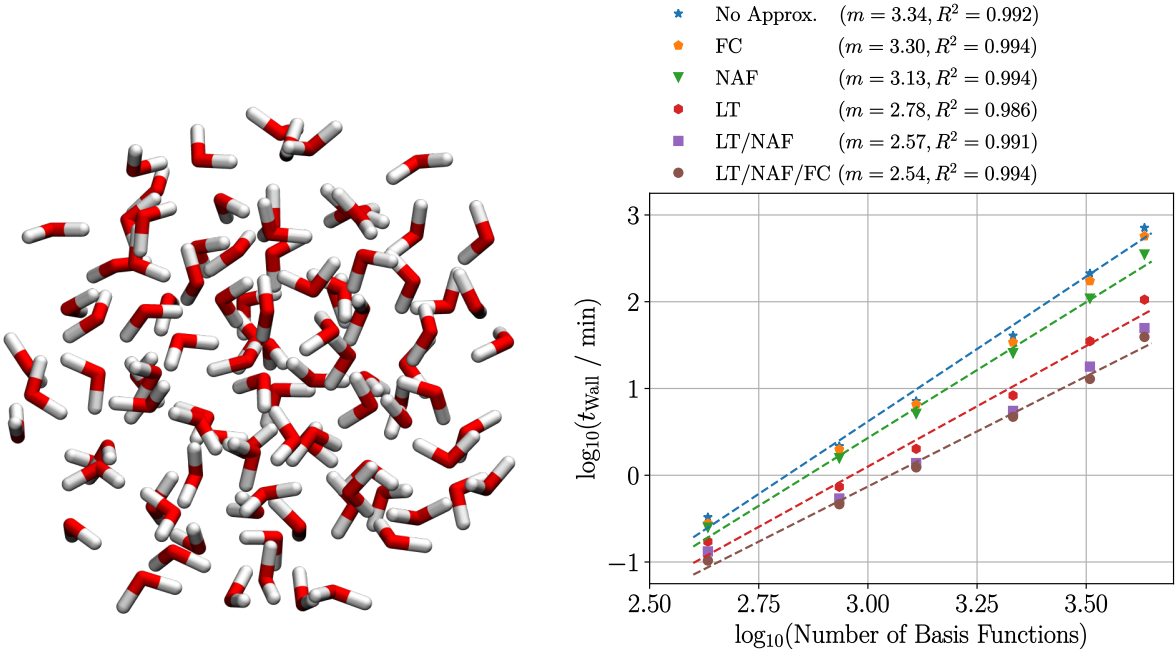


Figure 3: Left: Water cluster containing 100 water molecules. Right: Wall-clock timings as a function of the number of SCF basis functions (double-logarithmic plot) as well as slopes m and coefficients of determination R^2 of linear fit functions.

a slope of 3.34 for the unmodified AC- G_0W_0 algorithm, which is only slightly smaller than the formal scaling exponent of four that would be expected for the AC approach. The exponent is reduced by both the FC and NAF approximations to 3.30 and 3.13, respectively, where no such reduction would be expected for the exponent but rather for the prefactor only. Here, we note that the number of NAFs included in the calculations is on average 25–30% lower than the number of original auxiliary basis functions. For the water cluster containing 100 water molecules, the auxiliary-basis size reduction is 26%, which should result in a speed-up of $0.74^{-2} \approx 1.83$, and which is close to the observed speed-up of 2.0. The LT approximation leads to a lowering of the exponent from 3.34 to 2.78. In this case, the expected speed-up should be proportional to the quotient of the original number of imaginary frequencies and the number of Laplace grid points (see Eq. 8). For the cluster containing 100 water molecules, this ratio is $128/17 \approx 7.5$ which compares well with the observed speed-up of 6.7. Inspecting the exponents of the two combined approximations LT/NAF as

# GL-Grid Points	32	10.4 17.6/3.7	9.5 6.2/1.9	9.5 4.4/1.4	7.4 4.7/1.5	6.3 4.7/1.5	5.0 4.7/1.4
	64	21.8 17.6/3.7	17.9 6.2/1.9	16.2 4.5/1.4	13.4 4.7/1.5	11.5 4.7/1.4	9.5 4.7/1.4
	128	35.1 17.6/3.7	29.3 6.2/1.9	30.2 4.5/1.4	24.1 4.7/1.5	20.5 4.7/1.4	17.2 4.7/1.4
		8	9	10	12	14	18
		# LT-Grid Points					

Figure 4: Comparison of the speed-up (blue) and deviation of the HOMO/LUMO quasi-particle energies (green, in eV), relative to AC- G_0W_0 for various Gauss–Legendre (GL) and LT grid sizes (in combination with FC/NAF) for a water cluster containing 100 water molecules.

well as LT/NAF/FC, we find that the individual reductions in computational scaling add up so that for LT/NAF/FC the slope of the linear fit (as a measure of the computational scaling) is lowered by almost one with respect to the regular AC- G_0W_0 calculation. For the presented wall-clock timings, it can thus be seen that, although the formal scaling behavior is unchanged by the approximations introduced, LT- G_0W_0 leads to a drastically lower practical computational scaling, because the onset of the asymptotic formal scaling of $\mathcal{O}(N^4)$ is delayed to larger systems than employed here, all while retaining a very high degree of accuracy. This makes LT-GW especially appealing for typical molecular quantum chemistry and also for subsystem DFT-based GW applications,²⁶ where the fragments are typically chosen to be of medium size.

As already indicated before, the thresholds for the numerical frequency integration and LT transformation are chosen conservatively. Therefore, a more in-depth comparison of accuracy and speed-up for various sizes of the modified GL-grid (32/64/128) and the LT-grid (8/9/10/12/14/18) in combination with the NAF and FC approximations are given in Fig. 4. The speed-ups range from 5.0 to 35.1 for a ratio of approximately 1.8 to 16 for the two grid sizes (resulting in a deviation in the HOMO/LUMO quasi-particle energies of

Table 3: Wall-clock timings (min) and speed-ups for the calculation of the screened Coulomb interaction W for G_0W_0 and eigenvalue-self-consistent GW (five cycles) calculations for the different approximations employed in this study. The largest water cluster consisting of 100 water molecules served as the test system.

	None	LT	NAF	FC	LT/NAF	LT/NAF/FC
G_0W_0						
Wall-clock time (min)	711.0	105.7	350.4	570.4	49.7	39.3
Speed-up wrt reference	1.0	6.7	2.0	1.2	14.3	18.1
evGW						
Wall-clock time (min)	3502.6	530.0	1692.0	2775.3	263.2	199.4
Speed-up wrt reference	1.0	6.6	2.1	1.3	13.3	17.6

4.7/1.4 and 17.6/3.7 eV, respectively). This indicates again that, even though the ratio of the two grid sizes is small, a five-fold speed-up can be achieved in combination with NAF and FC because the total speed-up is the result of the product of the different contributions (LT/FC/NAF). For the remaining part of the manuscript we keep the default settings for the LT- and GL-grid as described in Sec. 3. These settings introduce negligible errors, while resulting in realistic speed-ups which are neither at the low end nor at the high end of the spectrum, as can be deduced from Fig. 4.

Additionally, we consider absolute timings of the G_0W_0 and eigenvalue-self-consistent GW (five cycles) calculations for the cluster containing 100 water molecules to illustrate the speed-up that can be expected in practical calculations with moderately sized systems and the LT- G_0W_0 method. The results can be found in Tab. 3. It turns out that the speed-ups of the composite approximation LT/NAF/FC are 18.1 and 17.6 for G_0W_0 and evGW, respectively, which slightly exceeds the product of the speed-ups of the individual LT (6.7 and 6.6), NAF (2.0 and 2.1), and FC (1.2 and 1.3) approximations, each amounting to roughly 16. The individual approximations thus do not interfere with each other but can constructively be used in combination, and the respective speed-up directly carries over to (partially) self-consistent GW calculations. Additionally, in Fig. S2 of the SI, we break down the computational time as a function of the size of the water cluster both for regular and

LT/NAF/FC-AC- G_0W_0 calculations into the contribution of (i) the three-center molecular-orbital integrals, (ii) the screened Coulomb interaction, and (iii) the NAF approximation (in the latter case). Further, we compare wall-clock timing contributions as a function of the employed CPU threads for the water cluster containing 100 water molecules in Tab. S3 of the SI. Finally, we note that the G_0W_0 calculation using only the LT approximation is about twice as fast as the regular one already for the smallest investigated water cluster containing 10 molecules (10 seconds vs 20 seconds), providing evidence for the small prefactor of LT-GW combined with the NAF and FC approximations.

4.2 LT- G_0W_0 with BSE

We apply a combination of LT- G_0W_0 and the Bethe–Salpeter (BSE) equation to investigate the effect of the LT approximation on the accuracy of linear absorption spectra. The BSE calculations are performed with the efficient integral-direct resolution of the identity implementation for the Hartree–Fock and long-range exchange part of the response matrix in SERENITY originally presented in our work in Ref. 62. As introduced above, the LT- G_0W_0 method refers to the application of the LT, NAF, and FC approximation and will be used in the following.

As a first test case, we consider the WW-6 dye relevant in photovoltaics.^{63,64} The molecular geometry was taken from Ref. 64 and is displayed in Fig. 5. Within the def2-TZVP basis set, there are 5583 SCF basis functions as well as 13802 auxiliary basis functions for the GW/BSE part of the calculation. In Fig. 5, we compare the linear absorption spectra for the WW-6 system that was obtained with the regular AC- G_0W_0 /BSE calculation with the LT- G_0W_0 calculation employing both the NAF ($\varepsilon_{\text{NAF}} = 10^{-2}$) and the FC approximations. In both cases, eight of the lowest-lying excitation energies and corresponding oscillator strengths were determined. The FC approximation was not applied for the BSE calculations. We find no visible difference between the linear absorption spectra calculated with the regular and the approximate approach. Numerical results for QP energies as well as excitation

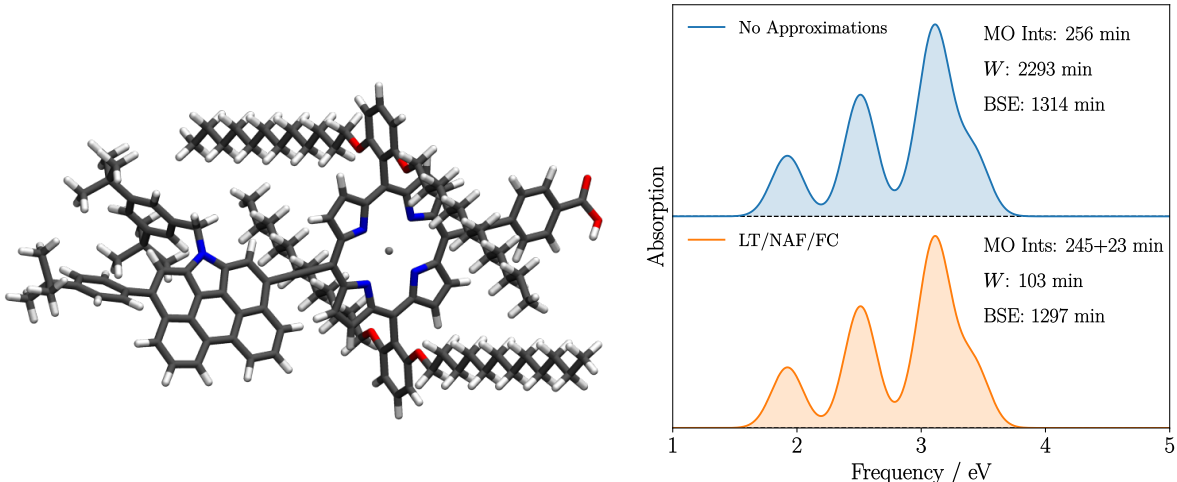


Figure 5: Comparison of linear absorption spectra obtained with a regular AC- G_0W_0 /BSE calculation and one where the set of LT/NAF/FC approximations is used for the G_0W_0 calculation. The largest portions of the computational wall-clock timings are additionally broken down [BHLYP/def2-TZVP]. The wall-clock time for the reference KS-DFT calculation was 136 minutes. The oscillator strengths were calculated in the dipole-length representation and broadened with Gaussian functions with a full width at half maximum of 0.3 eV.

energies and oscillator strengths can be found in Tabs. 4 and 5, respectively. The mean deviation of QP energies is about 9.6 meV which far exceeds the mean error of excitation energies and oscillator strengths which amount to 0.75 meV and $0.39 \cdot 10^{-3}$ a.u., respectively. The occupied and virtual QP energy errors are more systematic for this test system than for the HOMOs and LUMOs of the water clusters investigated beforehand. This results in more favorable error cancellation for excitation energies, which depend on QP energy differences. The errors of the oscillator strengths are equally negligible, which, in turn, is probably a result of the eigenvectors of the BSE problem being largely unaffected because of the error cancellation mentioned above.

Inspecting the computational timings (given in Fig. 5), we find that in the regular case, the overall wall-clock timings are dominated by the calculation of the screened Coulomb interaction W with 2293 minutes, while in the approximate case, the BSE part of the calculation exceeds the time needed for the GW calculation by far. Here, the overall G_0W_0 calculation time is, in fact, dominated by the preparation of the three-index MO integrals,

Table 4: Quasi-particle (QP) energies of the regular WW-6 G_0W_0 calculation (ϵ), QP energies of the LT/NAF/FC- G_0W_0 calculation ($\tilde{\epsilon}$) as well as their deviation (BHLYP/def2-TZVP, MAE: mean-absolute error).

	ϵ / eV	$\tilde{\epsilon} / \text{eV}$	$\Delta\epsilon / \text{meV}$
HOMO-4	-7.5346	-7.5262	8.3
HOMO-3	-7.1752	-7.1662	9.0
HOMO-2	-6.4024	-6.3932	9.2
HOMO-1	-6.2786	-6.2691	9.5
HOMO	-5.8659	-5.8564	9.5
LUMO	-1.8539	-1.8438	10.0
LUMO+1	-1.3771	-1.3670	10.1
LUMO+2	-0.9054	-0.8951	10.3
LUMO+3	-0.3816	-0.3717	9.9
LUMO+4	0.1719	0.1821	10.2
MAE			9.6

as the calculation of W only took 103 minutes. We also note that for the approximate calculation, setting up the NAF matrix, diagonalizing it, and then performing the NAF transformation to the three-index integral tensor introduces a small overhead of about 25 minutes (or ten percent), which is summarized in the timings for the ‘‘MO Ints’’. The number of NAFs included in the calculation was 8755 corresponding to a reduction of 37% with respect to the full number of auxiliary basis functions. The speed-up for the entire calculation amounts to 2.3 (3915 minutes vs 1720 minutes) while the speed-up for the calculation of the screened Coulomb interaction alone is 22.3 (2293 minutes vs 103 minutes). These calculations demonstrate that LT-GW is able to provide accurate references for BSE calculations, while drastically reducing the computational demand of the preceding G_0W_0 calculation.

As a second test system, we consider stacks of BODIPY dyes, which are of interest in the field of supramolecular polymer design.^{65,66} Additionally, supermolecular BODIPY-based compounds are interesting for GW/BSE calculations in particular because alternative (standard) methods for predicting their absorption spectra may either lack the necessary accuracy (e.g. linear response time-dependent density-functional theory, see e.g. Ref. 67) or are simply not feasible for this kind of system size (e.g. coupled cluster-based methodology

Table 5: Excitation energies (ω_{0n}) and oscillator strengths (f_{0n}) of the regular G_0W_0 /BSE calculation and the LT/NAF/FC- G_0W_0 /BSE calculation (indicated by a tilde) and the resulting deviation (BHLYP/def2-TZVP, MAE: mean-absolute error).

$0 \rightarrow n$	ω_n / eV	$\tilde{\omega}_n / \text{eV}$	$\Delta\omega_n / \text{meV}$	f_n	\tilde{f}_n	$\Delta f_n / 10^{-3}$
1	1.9220	1.9225	0.53	0.8508	0.8510	0.20
2	1.9997	2.0002	0.52	0.0103	0.0103	0.01
3	2.5107	2.5114	0.69	1.7237	1.7247	0.99
4	2.9090	2.9098	0.77	0.1397	0.1396	-0.09
5	3.0747	3.0754	0.62	0.5167	0.5172	0.47
6	3.1149	3.1157	0.86	2.1007	2.1017	0.99
7	3.2286	3.2297	1.07	0.0537	0.0536	-0.02
8	3.4163	3.4172	0.91	0.9013	0.9017	0.37
MAE			0.75			0.39

such as coupled cluster with singles and approximate doubles⁶⁸ and even local variants thereof^{69,70}). In our calculations, we include monomer, dimer, and tetramer geometries (provided by the authors of Ref. 65 and displayed in Fig. 6) and compare our G_0W_0 /BSE-based spectra with experimental ones in Fig. 6. For all n -mers, 32 of the lowest-lying excitation energies and corresponding oscillator strengths were determined after calculating 20 of both the lowest-lying virtual and highest-lying occupied QP energies for each monomer in each geometry, that is, 40 for the dimer as well as 80 for the tetramer. Based on the findings of the approximate calculations for the WW-6 test system, we omit G_0W_0 calculations that do not apply any further approximations here.

The experimental spectra exhibit three main bands at about 600, 400, and 300 nm. Interestingly, a strong blue shift of, in particular, the energetically lowest-lying absorption band is observed upon aggregation (experimentally induced by lowering the solution temperature). This behavior can most likely be attributed to the corresponding interaction of the transition dipole moments of the monomers in this stacking pattern. Going over to the computed spectra, one finds that the monomer spectrum reproduces the position and intensity of the experimental bands with a high degree of accuracy (given a constant shift of the absorption spectrum of 0.48 eV). It can further be seen that the blue shift of the

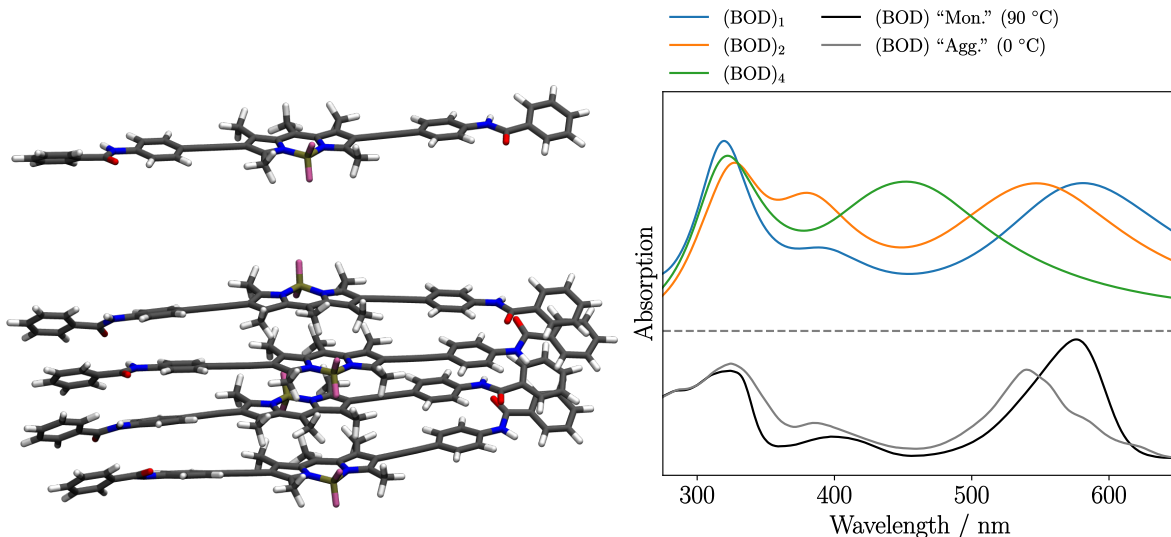


Figure 6: Left: BODIPY-based dyes in monomeric (upper) and tetrameric form (lower) (geometries provided by the authors of Ref. 65). Right: Comparison of linear absorption spectra obtained with LT-GW [BHLYP/def2-TZVP/NAF/FC] with experimental absorption spectra originally presented in Ref. 65, which were generated from raw data provided by the authors from that article. The experimental monomer (“Mon.”) and aggregate (“Agg.”) spectra were obtained by varying the solution temperature assuming that for very high and low temperatures, respectively, mainly the monomeric and aggregated form exist. The shown spectra correspond to the coldest and hottest solution temperatures investigated in Ref. 65, namely 0 and 90 °C. While methylcyclohexane was used as a solvent experimentally, we performed vacuum calculations. The oscillator strengths were calculated in the dipole-length representation and broadened with Gaussian functions with a full width at half maximum of 0.3 eV. The absorption spectra were subsequently red-shifted by 0.48 eV and converted to the wavelength domain.

lowest-lying absorption band of the dimer compares well with the experimental one. The computed tetramer spectrum exhibits a blue shift far exceeding the experimental one. This is most likely due to a combination of different factors. On the one hand, the experimental spectrum is a combination of several different aggregates of varying sizes and particular arrangements. On the other hand, the tetramer geometry was obtained by stacking two dimers on top of each other followed by a reoptimization. As a result, the distance between the inner two monomers is smaller than the distance between the outer pairs which could lead to an overestimation of the excitonic couplings leading to the blue shift. The GW calculation (screened Coulomb interaction W) took 6, 70, and 813 minutes for the monomer, dimer, and

tetramer, respectively.

5 Conclusion

We have presented the LT-GW method, for which we numerically demonstrated that it follows our three main objectives: (a) a small prefactor, (b) minimal effort for adaptation in existing AC-GW codes, and (c) significant performance improvements (up to 22-fold) for a wide range of system sizes with controllable error. For this, LT-GW combines the GW approximation in the context of the analytic continuation (AC) approach with a Laplace transformation (LT), natural auxiliary functions (NAFs), and the frozen-core (FC) approximation. We have highlighted its synergy with the BSE for calculations of excitation energy and properties for extended systems consisting of up to 7412 basis functions. We are convinced that the LT-GW method constitutes a practical and widely applicable extension to existing GW implementations for molecular systems.

In the LT-G₀W₀/BSE calculations, we have shown that the computational time is now dominated by the BSE calculation. Based on our three guiding principles, we aim to achieve similar improvements also for the BSE in the future by making use of, for example, minimal auxiliary basis sets⁷¹ or simplified integrals.^{72,73}

Supporting Information Available

HOMO and LUMO quasi-particle energies for molecular systems of the GW100 benchmark set, non-logarithmic wall-clock-timings and the speed-up plot of the water clusters, wall-clock-timings contributions for the water clusters, and wall-clock timings as a function of employed CPU threads for the water cluster containing 100 molecules can be found in the Supporting Information.

The data supporting the findings of this study are available either within the supplementary material or upon reasonable request from the authors.

Acknowledgement

J.T. gratefully acknowledges funding by the Deutsche Forschungsgemeinschaft (DFG, German Research Foundation) through DFG-495279997. N.N. and J.N. gratefully acknowledge funding by the DFG through SFB 1459 (Project A03, Project-ID A03-433682494). We would like to thank Christian Mück-Lichtenfeld for providing the monomer, dimer, and tetramer BODIPY geometries originally presented in Ref. 65. We would like to thank Alexander Rödle and Gustavo Fernández for providing the raw data of the experimental absorption spectra originally presented in Ref. 65.

References

- (1) Hedin, L. New method for calculating the one-particle Green's function with application to the electron-gas problem. *Phys. Rev.* **1965**, *139*, A796.
- (2) Onida, G.; Reining, L.; Godby, R.; Del Sole, R.; Andreoni, W. Ab initio calculations of the quasiparticle and absorption spectra of clusters: the sodium tetramer. *Phys. Rev. Lett.* **1995**, *75*, 818.
- (3) Rohlfing, M.; Louie, S. G. Excitonic effects and the optical absorption spectrum of hydrogenated Si clusters. *Phys. Rev. Lett.* **1998**, *80*, 3320.
- (4) Albrecht, S.; Reining, L.; Del Sole, R.; Onida, G. Ab initio calculation of excitonic effects in the optical spectra of semiconductors. *Phys. Rev. Lett.* **1998**, *80*, 4510.
- (5) Rohlfing, M.; Louie, S. G. Electron-hole excitations in semiconductors and insulators. *Phys. Rev. Lett.* **1998**, *81*, 2312.
- (6) Benedict, L. X.; Shirley, E. L.; Bohn, R. B. Optical absorption of insulators and the electron-hole interaction: An ab initio calculation. *Phys. Rev. Lett.* **1998**, *80*, 4514.

- (7) Rohlfing, M.; Louie, S. G. Electron-hole excitations and optical spectra from first principles. *Phys. Rev. B* **2000**, *62*, 4927.
- (8) Baumeier, B.; Andrienko, D.; Ma, Y.; Rohlfing, M. Excited states of dicyanovinyl-substituted oligothiophenes from many-body Green’s functions theory. *J. Chem. Theory Comput.* **2012**, *8*, 997–1002.
- (9) Ren, X.; Rinke, P.; Blum, V.; Wieferink, J.; Tkatchenko, A.; Sanfilippo, A.; Reuter, K.; Scheffler, M. Resolution-of-identity approach to Hartree–Fock, hybrid density functionals, RPA, MP2 and GW with numeric atom-centered orbital basis functions. *New J. Phys.* **2012**, *14*, 053020.
- (10) van Setten, M. J.; Weigend, F.; Evers, F. The GW-method for quantum chemistry applications: theory and implementation. *J. Chem. Theory Comput.* **2013**, *9*, 232–246.
- (11) Jacquemin, D.; Duchemin, I.; Blase, X. Benchmarking the Bethe–Salpeter formalism on a standard organic molecular set. *J. Chem. Theory Comput.* **2015**, *11*, 3290–3304.
- (12) Bruneval, F.; Rangel, T.; Hamed, S. M.; Shao, M.; Yang, C.; Neaton, J. B. molgw 1: Many-body perturbation theory software for atoms, molecules, and clusters. *Comput. Phys. Commun.* **2016**, *208*, 149–161.
- (13) Wilhelm, J.; Del Ben, M.; Hutter, J. GW in the Gaussian and plane waves scheme with application to linear acenes. *J. Chem. Theory Comput.* **2016**, *12*, 3623–3635.
- (14) Krause, K.; Klopper, W. Implementation of the Bethe–Salpeter equation in the TURBOMOLE program. *J. Comput. Chem.* **2017**, *38*, 383–388.
- (15) Golze, D.; Wilhelm, J.; van Setten, M. J.; Rinke, P. Core-level binding energies from GW: An efficient full-frequency approach within a localized basis. *J. Chem. Theory Comput.* **2018**, *14*, 4856–4869.

- (16) Balasubramani, S. G.; Chen, G. P.; Coriani, S.; Diedenhofen, M.; Frank, M. S.; Franzke, Y. J.; Furche, F.; Grotjahn, R.; Harding, M. E.; Hättig, C., et al. TURBO-MOLE: Modular program suite for ab initio quantum-chemical and condensed-matter simulations. *J. Chem. Phys.* **2020**, *152*, 184107.
- (17) Förster, A.; Visscher, L. Low-Order Scaling G0W0 by Pair Atomic Density Fitting. *J. Chem. Theory Comput.* **2020**,
- (18) Liu, C.; Kloppenburg, J.; Yao, Y.; Ren, X.; Appel, H.; Kanai, Y.; Blum, V. All-electron ab initio Bethe-Salpeter equation approach to neutral excitations in molecules with numeric atom-centered orbitals. *J. Chem. Phys.* **2020**, *152*, 044105.
- (19) Zhang, M.; Liu, Y.; Jiang, Y.-n.; Ma, Y. Many-Body Green's Function Theory for Electronic Excitations in Complex Chemical Systems. *J. Phys. Chem. Lett.* **2023**, *14*, 5267–5282.
- (20) Fiesta website. <http://perso.neel.cnrs.fr/xavier.blase/fiesta/index.html>, 2023; (accessed May 19 2023).
- (21) Sun, Q.; Zhang, X.; Banerjee, S.; Bao, P.; Barbry, M.; Blunt, N. S.; Bogdanov, N. A.; Booth, G. H.; Chen, J.; Cui, Z.-H., et al. Recent developments in the PySCF program package. *J. Chem. Phys.* **2020**, *153*, 024109.
- (22) Zhu, T.; Chan, G. K.-L. All-electron Gaussian-based G 0 W 0 for valence and core excitation energies of periodic systems. *J. Chem. Theory Comput.* **2021**, *17*, 727–741.
- (23) Unsleber, J. P.; Dresselhaus, T.; Klahr, K.; Schnieders, D.; Böckers, M.; Barton, D.; Neugebauer, J. Serenity: A subsystem quantum chemistry program. *J. Comput. Chem.* **2018**, *39*, 788.
- (24) Niemeyer, N.; Eschenbach, P.; Bensberg, M.; Tölle, J.; Hellmann, L.; Lampe, L.; Mas-

- solle, A.; Rikus, A.; Schnieders, D.; Unsleber, J. P., et al. The subsystem quantum chemistry program Serenity. *Wiley Interdiscip. Rev. Comput. Mol. Sci.* **2022**, e1647.
- (25) Barton, D. et al. qcserenity/serenity: Release 1.5.2. 2023; <https://doi.org/10.5281/zenodo.7759804>.
- (26) Tölle, J.; Deilmann, T.; Rohlfing, M.; Neugebauer, J. Subsystem-Based GW/Bethe–Salpeter Equation. *J. Chem. Theory Comput.* **2021**, *17*, 2186–2199.
- (27) Förster, A.; Visscher, L. Low-Order Scaling Quasiparticle Self-Consistent GW for Molecules. *Front. Chem.* **2021**, 698.
- (28) Tirimbo, G.; Sundaram, V.; Caylak, O.; Scharpach, W.; Sijen, J.; Junghans, C.; Brown, J.; Ruiz, F. Z.; Renaud, N.; Wehner, J., et al. Excited-state electronic structure of molecules using many-body Green’s functions: Quasiparticles and electron–hole excitations with VOTCA-XTP. *J. Chem. Phys.* **2020**, *152*, 114103.
- (29) Apra, E.; Bylaska, E. J.; De Jong, W. A.; Govind, N.; Kowalski, K.; Straatsma, T. P.; Valiev, M.; van Dam, H. J.; Alexeev, Y.; Anchell, J., et al. NWChem: Past, present, and future. *J. Chem. Phys.* **2020**, *152*, 184102.
- (30) Mejia-Rodriguez, D.; Kunitsa, A.; Aprà, E.; Govind, N. Scalable Molecular GW Calculations: Valence and Core Spectra. *J. Chem. Theory Comput.* **2021**, *17*, 7504–7517.
- (31) Bruneval, F.; Dattani, N.; Van Setten, M. J. The GW Miracle in Many-Body Perturbation Theory for the Ionization Potential of Molecules. *Front. Chem.* **2021**, *9*.
- (32) Golze, D.; Dvorak, M.; Rinke, P. The GW compendium: A practical guide to theoretical photoemission spectroscopy. *Front. Chem.* **2019**, *7*, 377.
- (33) Settels, V.; Liu, W.; Pflaum, J.; Fink, R. F.; Engels, B. Comparison of the electronic structure of different perylene-based dye-aggregates. *J. Comput. Chem.* **2012**, *33*, 1544–1553.

- (34) Bruneval, F. Ionization energy of atoms obtained from GW self-energy or from random phase approximation total energies. *J. Chem. Phys.* **2012**, *136*, 194107.
- (35) Wilhelm, J.; Golze, D.; Talirz, L.; Hutter, J.; Pignedoli, C. A. Toward GW calculations on thousands of atoms. *J. Chem. Phys. Lett.* **2018**, *9*, 306–312.
- (36) Godby, R. W.; Schlüter, M.; Sham, L. Self-energy operators and exchange-correlation potentials in semiconductors. *Phys. Rev. B* **1988**, *37*, 10159.
- (37) Holzer, C.; Klopper, W. Ionized, electron-attached, and excited states of molecular systems with spin-orbit coupling: Two-component GW and Bethe-Salpeter implementations. *J. Chem. Phys.* **2019**, *150*, 204116.
- (38) Rojas, H.; Godby, R. W.; Needs, R. Space-time method for ab initio calculations of self-energies and dielectric response functions of solids. *Phys. Rev. Lett.* **1995**, *74*, 1827.
- (39) Liu, P.; Kaltak, M.; Klimeš, J.; Kresse, G. Cubic scaling GW: Towards fast quasiparticle calculations. *Phys. Rev. B* **2016**, *94*, 165109.
- (40) Wilhelm, J.; Seewald, P.; Golze, D. Low-scaling GW with benchmark accuracy and application to phosphorene nanosheets. *J. Chem. Theory Comput.* **2021**, *17*, 1662–1677.
- (41) Förster, A.; Visscher, L. GW100: A Slater-Type Orbital Perspective. *J. Chem Theory Comput.* **2021**, *17*, 5080–5097.
- (42) Duchemin, I.; Blase, X. Cubic-scaling all-electron GW calculations with a separable density-fitting space-time approach. *J. Chem. Theory Comput.* **2021**, *17*, 2383–2393.
- (43) Kaltak, M.; Klimes, J.; Kresse, G. Low scaling algorithms for the random phase approximation: Imaginary time and Laplace transformations. *J. Chem. Theory Comput.* **2014**, *10*, 2498–2507.

- (44) Duchemin, I.; Blase, X. Separable resolution-of-the-identity with all-electron Gaussian bases: Application to cubic-scaling RPA. *J. Chem. Phys.* **2019**, *150*.
- (45) Almlöf, J. Elimination of energy denominators in Møller–Plesset perturbation theory by a Laplace transform approach. *Chem. Phys. Lett.* **1991**, *181*, 319–320.
- (46) Häser, M.; Almlöf, J. Laplace transform techniques in Møller–Plesset perturbation theory. *J. Chem. Phys.* **1992**, *96*, 489–494.
- (47) Häser, M. Møller–Plesset (MP2) perturbation theory for large molecules. *Theor. Chem. Acc.* **1993**, *87*, 147–173.
- (48) Kállay, M. A systematic way for the cost reduction of density fitting methods. *J. Chem. Phys.* **2014**, *141*, 244113.
- (49) Mester, D.; Nagy, P. R.; Kállay, M. Reduced-cost linear-response CC2 method based on natural orbitals and natural auxiliary functions. *J. Chem. Phys.* **2017**, *146*, 194102.
- (50) Vidberg, H.; Serene, J. Solving the Eliashberg equations by means of N-point Padé approximants. *J. Low Temp. Phys.* **1977**, *29*, 179–192.
- (51) Weigend, F.; Ahlrichs, R. Balanced basis sets of split valence, triple zeta valence and quadruple zeta valence quality for H to Rn: Design and assessment of accuracy. *Phys. Chem. Chem. Phys.* **2005**, *7*, 3297–3305.
- (52) Weigend, F.; Häser, M.; Patzelt, H.; Ahlrichs, R. RI-MP2: optimized auxiliary basis sets and demonstration of efficiency. *Chem. Phys. Lett.* **1998**, *294*, 143–152.
- (53) Weigend, F. Accurate Coulomb-fitting basis sets for H to Rn. *Phys. Chem. Chem. Phys.* **2006**, *8*, 1057–1065.
- (54) Takatsuka, A.; Ten-No, S.; Hackbusch, W. Minimax approximation for the decomposition of energy denominators in Laplace-transformed Møller–Plesset perturbation theories. *J. Chem. Phys.* **2008**, *129*, 044112.

- (55) Helmich-Paris, B.; Visscher, L. Improvements on the minimax algorithm for the Laplace transformation of orbital energy denominators. *J. Comput. Phys.* **2016**, *321*, 927–931.
- (56) Winter, N. O.; Hättig, C. Scaled opposite-spin CC2 for ground and excited states with fourth order scaling computational costs. *J. Chem. Phys.* **2011**, *134*, 184101.
- (57) ORCA Input Library. <https://sites.google.com/site/orcainputlibrary/frozen-core-calculations>, 2023; (accessed May 19 2023).
- (58) van Setten, M. J.; Caruso, F.; Sharifzadeh, S.; Ren, X.; Scheffler, M.; Liu, F.; Lischner, J.; Lin, L.; Deslippe, J. R.; Louie, S. G.; Yang, C.; Weigend, F.; Neaton, J. B.; Evers, F.; Rinke, P. GW 100: Benchmarking G 0 W 0 for molecular systems. *J. Chem. Theory Comput.* **2015**, *11*, 5665–5687.
- (59) matplotlib.pyplot.boxplot Documentation Entry. https://matplotlib.org/3.1.1/api/_as_gen/matplotlib.pyplot.boxplot.html, 2023; (accessed July 10 2023).
- (60) Humphrey, W.; Dalke, A.; Schulten, K. VMD – Visual Molecular Dynamics. *J. Mol. Graph.* **1996**, *14*, 33–38.
- (61) Bannwarth, C.; Ehlert, S.; Grimme, S. GFN2-xTB—An accurate and broadly parametrized self-consistent tight-binding quantum chemical method with multipole electrostatics and density-dependent dispersion contributions. *J. Chem. Theory. Comput.* **2019**, *15*, 1652–1671.
- (62) Hellmann, L.; Tölle, J.; Niemeyer, N.; Neugebauer, J. Automated generation of optimized auxiliary basis sets for long-range-corrected TDDFT using the Cholesky decomposition. *J. Chem. Theory Comput.* **2022**, *18*, 2959–2974.
- (63) Mester, D.; Nagy, P. R.; Kállay, M. Reduced-scaling correlation methods for the excited states of large molecules: Implementation and benchmarks for the second-order

- algebraic-diagrammatic construction approach. *J. Chem. Theory Comput.* **2019**, *15*, 6111–6126.
- (64) Luo, J.; Xu, M.; Li, R.; Huang, K.-W.; Jiang, C.; Qi, Q.; Zeng, W.; Zhang, J.; Chi, C.; Wang, P., et al. N-annulated perylene as an efficient electron donor for porphyrin-based dyes: enhanced light-harvesting ability and high-efficiency Co (II/III)-based dye-sensitized solar cells. *J. Am. Chem. Soc.* **2014**, *136*, 265–272.
- (65) Rödle, A.; Ritschel, B.; Mück-Lichtenfeld, C.; Stepanenko, V.; Fernández, G. Influence of ester versus amide linkers on the supramolecular polymerization mechanisms of planar BODIPY dyes. *Chem. Eur. J.* **2016**, *22*, 15772–15777.
- (66) Aida, T.; Meijer, E. Supramolecular polymers—we’ve come full circle. *Isr. J. Chem.* **2020**, *60*, 33–47.
- (67) Momeni, M. R.; Brown, A. Why do TD-DFT excitation energies of BODIPY/aza-BODIPY families largely deviate from experiment? Answers from electron correlated and multireference methods. *J. Chem. Theory Comput.* **2015**, *11*, 2619–2632.
- (68) Christiansen, O.; Koch, H.; Jørgensen, P. The second-order approximate coupled cluster singles and doubles model CC2. *Chem. Phys. Lett.* **1995**, *243*, 409–418.
- (69) Berraud-Pache, R.; Neese, F.; Bistoni, G.; Izsák, R. Unveiling the photophysical properties of boron-dipyrromethene dyes using a new accurate excited state coupled cluster method. *J. Chem. Theory and Comput.* **2019**, *16*, 564–575.
- (70) Feldt, M.; Brown, A. Assessment of local coupled cluster methods for excited states of BODIPY/Aza-BODIPY families. *J. Comput. Chem.* **2021**, *42*, 144–155.
- (71) Zhou, Z.; Della Sala, F.; Parker, S. M. Minimal auxiliary basis set approach for the electronic excitation spectra of organic molecules. *J. Phys. Chem. Lett.* **2023**, *14*, 1968–1976.

- (72) Grimme, S. A simplified Tamm-Dancoff density functional approach for the electronic excitation spectra of very large molecules. *J. Chem. Phys.* **2013**, *138*, 244104.
- (73) Cho, Y.; Bintrim, S. J.; Berkelbach, T. C. Simplified GW/BSE Approach for Charged and Neutral Excitation Energies of Large Molecules and Nanomaterials. *J. Chem. Theory and Comput.* **2022**, *18*, 3438–3446.

Accelerating Analytic-Continuation GW Calculations with a Laplace Transformation and Natural Auxiliary Functions

– Supporting Information –

Johannes Tölle^{1,‡*}, Niklas Niemeyer^{2,‡}, and Johannes Neugebauer^{2†}

¹Division of Chemistry and Chemical Engineering,
California Institute of Technology, Pasadena, California 91125, USA

²University of Münster, Organisch-Chemisches Institut and
Center for Multiscale Theory and Computation,
Corrensstraße 36, 48149 Münster, Germany

[‡]Both authors contributed equally.

Date: November 16, 2023

*email: jtolle@caltech.edu

†email: j.neugebauer@uni-muenster.de

S1 GW100 Benchmark

Table S1: G_0W_0 HOMO quasi-particle energies for the molecular systems from the GW100 benchmark set for various approximations in the evaluation of the G_0W_0 self-energy relative to the “fully-analytic” approach without employing the RI approximation. Effective core potentials are used for the heavy elements rubidium, silver, xenon, and iodine. Analytic-RI: “Fully-analytic” approach using the RI approximation, AC: AC- G_0W_0 , LT: AC- G_0W_0 in combination with AC-LT ($\varepsilon_{LT} = 10^{-7}$), AC-FC: AC- G_0W_0 in combination with FC, AC-NAF: AC- G_0W_0 in combination with the NAF approximation ($\varepsilon_{NAF} = 10^{\{-6,-4,-2\}}$), AC-FC-LT-NAF: Combining AC- G_0W_0 with FC/LT/NAF ($\varepsilon_{LT} = 10^{-7}$, $\varepsilon_{NAF} = 10^{\{-6,-4,-2\}}$) [def2-TZVP, starting from Hartree–Fock orbitals]. This data is additionally provided as a text file.

	Analytic RI	AC	AC-FC	AC-LT	AC-NAF(6)	AC-NAF(4)	AC-NAF(2)	AC-LT-FC-NAF(6)	AC-LT-FC-NAF(4)	AC-LT-FC-NAF(2)	Analytic
butane	-12.074	-12.074	-12.069	-12.074	-12.074	-12.074	-12.073	-12.069	-12.069	-12.068	-12.076
carbon tetrabromide	-10.728	-10.728	-10.808	-10.728	-10.728	-10.728	-10.727	-10.808	-10.808	-10.807	-10.726
hydrogen peroxide	-11.987	-11.987	-11.984	-11.987	-11.987	-11.987	-11.987	-11.983	-11.983	-11.983	-11.989
thymine	-9.596	-9.596	-9.589	-9.596	-9.596	-9.596	-9.595	-9.589	-9.589	-9.588	-9.596
fluorine	-16.265	-16.265	-16.264	-16.265	-16.265	-16.265	-16.265	-16.264	-16.264	-16.263	-16.266
toluene	-9.069	-9.069	-9.062	-9.069	-9.069	-9.069	-9.068	-9.062	-9.062	-9.061	-9.069
ethylbenzene	-9.038	-9.038	-9.031	-9.038	-9.038	-9.038	-9.037	-9.031	-9.031	-9.030	-9.038
arsenic dimer	-9.704	-9.704	-9.759	-9.704	-9.704	-9.704	-9.704	-9.759	-9.759	-9.759	-9.705
ethane	-13.036	-13.036	-13.033	-13.036	-13.036	-13.036	-13.033	-13.033	-13.033	-13.030	-13.037
benzene	-9.438	-9.438	-9.431	-9.438	-9.438	-9.438	-9.437	-9.431	-9.431	-9.430	-9.438
sulfur tetrafluoride	-13.214	-13.214	-13.222	-13.214	-13.214	-13.214	-13.214	-13.222	-13.222	-13.221	-13.213
tetracarbon	-11.557	-11.557	-11.554	-11.557	-11.557	-11.557	-11.556	-11.554	-11.554	-11.553	-11.557
fluoroborane	-11.264	-11.264	-11.260	-11.264	-11.264	-11.264	-11.263	-11.260	-11.260	-11.259	-11.264
potassium bromide	-8.176	-8.176	-8.241	-8.176	-8.176	-8.176	-8.175	-8.241	-8.241	-8.239	-8.176
cytosine	-9.199	-9.199	-9.193	-9.199	-9.199	-9.199	-9.199	-9.193	-9.193	-9.192	-9.200
krypton	-13.968	-13.968	-14.049	-13.968	-13.968	-13.968	-13.968	-14.049	-14.049	-14.049	-13.968
diborane(6)	-12.667	-12.667	-12.665	-12.667	-12.667	-12.667	-12.667	-12.665	-12.665	-12.665	-12.669
water	-12.778	-12.778	-12.775	-12.778	-12.778	-12.778	-12.777	-12.774	-12.774	-12.773	-12.780
formic acid	-11.878	-11.878	-11.875	-11.878	-11.878	-11.878	-11.877	-11.875	-11.875	-11.874	-11.879
propane	-12.484	-12.484	-12.481	-12.484	-12.484	-12.484	-12.482	-12.481	-12.481	-12.479	-12.486
phosphine	-10.683	-10.683	-10.691	-10.683	-10.683	-10.683	-10.681	-10.691	-10.690	-10.689	-10.685
aniline	-8.258	-8.258	-8.250	-8.258	-8.258	-8.258	-8.257	-8.250	-8.250	-8.249	-8.257
carbon monoxide	-15.003	-15.003	-14.999	-15.003	-15.003	-15.003	-15.002	-14.999	-14.999	-14.998	-15.004
lithium hydride	-7.944	-7.944	-7.944	-7.944	-7.944	-7.944	-7.940	-7.944	-7.944	-7.940	-7.946
sodium hexamer	-4.413	-4.413	-4.413	-4.413	-4.413	-4.413	-4.409	-4.413	-4.413	-4.409	-4.414
magnesium fluoride	-13.790	-13.790	-13.789	-13.790	-13.790	-13.790	-13.788	-13.789	-13.789	-13.787	-13.791
sulfur dioxide	-12.872	-12.872	-12.875	-12.872	-12.872	-12.872	-12.872	-12.875	-12.875	-12.874	-12.872
disilane	-10.978	-10.978	-10.995	-10.978	-10.978	-10.978	-10.977	-10.995	-10.995	-10.993	-10.978
copper dimer	-6.991	-6.991	-6.992	-6.991	-6.991	-6.991	-6.989	-6.992	-6.992	-6.990	-6.992

ozone	-10.953	-10.953	-10.949	-10.953	-10.953	-10.953	-10.952	-10.949	-10.949	-10.947	-10.955
nitrogen	-17.072	-17.072	-17.067	-17.072	-17.072	-17.072	-17.072	-17.067	-17.067	-17.066	-17.074
ammonia	-11.089	-11.089	-11.085	-11.089	-11.089	-11.089	-11.088	-11.085	-11.085	-11.084	-11.088
acetaldehyde	-10.722	-10.722	-10.719	-10.722	-10.722	-10.722	-10.721	-10.719	-10.719	-10.717	-10.724
hydrogen sulfide	-10.413	-10.413	-10.426	-10.413	-10.413	-10.413	-10.412	-10.426	-10.426	-10.425	-10.415
sodium chloride	-9.156	-9.156	-9.173	-9.156	-9.156	-9.156	-9.155	-9.173	-9.173	-9.170	-9.157
phosphorus dimer	-10.473	-10.473	-10.482	-10.473	-10.473	-10.473	-10.472	-10.482	-10.482	-10.481	-10.475
ethylene	-10.685	-10.685	-10.678	-10.685	-10.685	-10.685	-10.684	-10.678	-10.678	-10.677	-10.686
methane	-14.633	-14.633	-14.630	-14.633	-14.633	-14.633	-14.631	-14.630	-14.630	-14.627	-14.634
cyclopentadiene	-8.777	-8.777	-8.770	-8.777	-8.777	-8.777	-8.776	-8.770	-8.770	-8.768	-8.778
hydrazine	-10.068	-10.068	-10.064	-10.068	-10.068	-10.068	-10.067	-10.064	-10.064	-10.063	-10.067
cyclopropane	-11.199	-11.199	-11.192	-11.199	-11.199	-11.199	-11.199	-11.192	-11.192	-11.191	-11.201
vinyl bromide	-9.997	-9.997	-10.027	-9.997	-9.997	-9.997	-9.996	-10.027	-10.027	-10.026	-9.997
potassium hydride	-6.099	-6.099	-6.100	-6.099	-6.099	-6.099	-6.099	-6.100	-6.100	-6.096	-6.100
silane	-13.078	-13.078	-13.092	-13.078	-13.078	-13.078	-13.077	-13.092	-13.092	-13.091	-13.079
guanine	-8.355	-8.355	-8.347	-8.355	-8.355	-8.355	-8.354	-8.347	-8.347	-8.346	-8.356
neon	-21.349	-21.349	-21.351	-21.349	-21.349	-21.349	-21.349	-21.350	-21.350	-21.350	-21.350
hydrogen cyanide	-13.821	-13.821	-13.814	-13.821	-13.821	-13.821	-13.820	-13.814	-13.814	-13.814	-13.822
boron nitride	-11.692	-11.692	-11.685	-11.692	-11.692	-11.692	-11.690	-11.685	-11.685	-11.683	-11.692
urea	-10.604	-10.604	-10.599	-10.604	-10.604	-10.604	-10.603	-10.599	-10.599	-10.598	-10.604
lithium fluoride	-11.251	-11.251	-11.250	-11.251	-11.251	-11.251	-11.248	-11.250	-11.250	-11.246	-11.252
helium	-24.294	-24.294	-24.294	-24.294	-24.294	-24.294	-24.294	-24.294	-24.294	-24.294	-24.294
acetylene	-11.530	-11.530	-11.524	-11.530	-11.530	-11.530	-11.529	-11.524	-11.524	-11.523	-11.532
ethoxy ethane	-10.377	-10.377	-10.374	-10.377	-10.377	-10.377	-10.375	-10.374	-10.374	-10.372	-10.377
hydrogen fluoride	-16.148	-16.148	-16.146	-16.148	-16.148	-16.148	-16.147	-16.146	-16.146	-16.146	-16.149
cyclooctatetraene	-8.588	-8.588	-8.581	-8.588	-8.588	-8.588	-8.587	-8.581	-8.581	-8.580	-8.587
pyridine	-9.830	-9.830	-9.823	-9.830	-9.830	-9.830	-9.829	-9.823	-9.823	-9.822	-9.830
carbon tetrachloride	-11.913	-11.913	-11.934	-11.913	-11.913	-11.913	-11.913	-11.934	-11.934	-11.932	-11.913
pentasilane	-9.705	-9.705	-9.722	-9.705	-9.705	-9.705	-9.704	-9.722	-9.722	-9.720	-9.703
uracil	-10.009	-10.009	-10.003	-10.009	-10.009	-10.009	-10.009	-10.003	-10.003	-10.002	-10.009
methanol	-11.460	-11.460	-11.457	-11.460	-11.460	-11.460	-11.459	-11.457	-11.457	-11.455	-11.461
borane	-13.528	-13.528	-13.526	-13.528	-13.528	-13.528	-13.528	-13.526	-13.526	-13.525	-13.530
carbon tetrafluoride	-16.792	-16.792	-16.791	-16.792	-16.792	-16.792	-16.792	-16.791	-16.791	-16.790	-16.793
vinyl chloride	-10.285	-10.285	-10.285	-10.285	-10.285	-10.285	-10.284	-10.285	-10.285	-10.284	-10.286
phenol	-8.823	-8.823	-8.815	-8.823	-8.823	-8.823	-8.822	-8.815	-8.815	-8.814	-8.823
aluminum fluoride	-15.577	-15.577	-15.588	-15.577	-15.577	-15.577	-15.576	-15.588	-15.588	-15.587	-15.578
carbon disulfide	-10.238	-10.238	-10.251	-10.238	-10.238	-10.238	-10.238	-10.251	-10.251	-10.250	-10.239
lithium dimer	-5.157	-5.157	-5.157	-5.157	-5.157	-5.157	-5.156	-5.157	-5.157	-5.156	-5.160
carbon dioxide	-14.164	-14.164	-14.160	-14.164	-14.164	-14.164	-14.163	-14.160	-14.160	-14.159	-14.165

phosphorus mononitride	-12.303	-12.303	-12.305	-12.303	-12.303	-12.303	-12.302	-12.305	-12.305	-12.304	-12.305
argon	-15.682	-15.682	-15.706	-15.682	-15.682	-15.682	-15.682	-15.706	-15.706	-15.704	-15.683
hydrogen azide	-11.029	-11.029	-11.024	-11.029	-11.029	-11.029	-11.029	-11.024	-11.024	-11.023	-11.029
hexafluorobenzene	-10.557	-10.557	-10.549	-10.557	-10.557	-10.557	-10.556	-10.549	-10.549	-10.548	-10.558
vinyl fluoride	-10.750	-10.750	-10.743	-10.750	-10.750	-10.750	-10.749	-10.743	-10.743	-10.742	-10.751
beryllium monoxide	-9.761	-9.761	-9.758	-9.761	-9.761	-9.761	-9.759	-9.758	-9.758	-9.757	-9.762
carbon oxysulfide	-11.474	-11.474	-11.483	-11.474	-11.474	-11.474	-11.473	-11.483	-11.483	-11.482	-11.475
formaldehyde	-11.268	-11.268	-11.265	-11.268	-11.268	-11.268	-11.267	-11.265	-11.265	-11.263	-11.269
ethanol	-11.172	-11.172	-11.169	-11.172	-11.172	-11.172	-11.171	-11.169	-11.169	-11.167	-11.173
bromine	-10.714	-10.714	-10.793	-10.714	-10.714	-10.714	-10.714	-10.793	-10.793	-10.792	-10.712
germane	-12.732	-12.732	-12.766	-12.732	-12.732	-12.732	-12.732	-12.766	-12.766	-12.765	-12.731
magnesium chloride	-11.851	-11.851	-11.868	-11.851	-11.851	-11.851	-11.850	-11.868	-11.868	-11.866	-11.852
carbon oxyselenide	-10.653	-10.653	-10.705	-10.653	-10.653	-10.653	-10.652	-10.705	-10.705	-10.705	-10.653
titanium fluoride	-16.048	-16.048	-16.047	-16.048	-16.048	-16.048	-16.048	-16.047	-16.047	-16.046	-16.048
copper cyanide	-11.187	-11.187	-11.183	-11.187	-11.187	-11.187	-11.186	-11.183	-11.183	-11.183	-11.188
sodium tetramer	-4.241	-4.241	-4.241	-4.241	-4.241	-4.241	-4.237	-4.241	-4.241	-4.237	-4.243
hydrogen chloride	-12.710	-12.710	-12.728	-12.710	-12.710	-12.710	-12.710	-12.728	-12.728	-12.727	-12.712
arsine	-10.495	-10.495	-10.553	-10.495	-10.495	-10.495	-10.494	-10.553	-10.553	-10.551	-10.499
magnesium monoxide	-8.383	-8.383	-8.382	-8.383	-8.383	-8.383	-8.380	-8.382	-8.382	-8.379	-8.384
dipotassium	-4.025	-4.025	-4.025	-4.025	-4.025	-4.025	-4.020	-4.025	-4.025	-4.020	-4.026
sodium dimer	-4.933	-4.933	-4.933	-4.933	-4.933	-4.933	-4.928	-4.933	-4.933	-4.928	-4.930
chlorine	-11.686	-11.686	-11.707	-11.686	-11.686	-11.686	-11.686	-11.707	-11.707	-11.705	-11.686
adenine	-8.624	-8.624	-8.616	-8.624	-8.624	-8.624	-8.623	-8.616	-8.616	-8.615	-8.624
gallium monochloride	-9.856	-9.856	-9.909	-9.856	-9.856	-9.856	-9.855	-9.909	-9.909	-9.909	-9.854
hydrogen	-16.304	-16.304	-16.304	-16.304	-16.304	-16.304	-16.304	-16.304	-16.304	-16.304	-16.306
dirubidium	-3.837	-3.837	-3.837	-3.837	-3.837	-3.837	-3.833	-3.837	-3.837	-3.833	-3.844
silver dimer	-6.963	-6.963	-6.963	-6.963	-6.963	-6.963	-6.960	-6.963	-6.963	-6.960	-6.964
xenon	-12.324	-12.324	-12.371	-12.324	-12.324	-12.324	-12.324	-12.371	-12.371	-12.371	-12.324
iodine	-9.674	-9.674	-9.717	-9.674	-9.674	-9.674	-9.673	-9.717	-9.717	-9.717	-9.672
vinyl iodide	-9.456	-9.456	-9.481	-9.456	-9.456	-9.456	-9.455	-9.481	-9.481	-9.481	-9.456
aluminum iodide	-9.970	-9.970	-10.013	-9.970	-9.970	-9.970	-9.968	-10.013	-10.013	-10.013	-9.969
carbon tetraiodide	-9.500	-9.500	-9.545	-9.500	-9.500	-9.500	-9.499	-9.545	-9.545	-9.545	-9.499

Table S2: G_0W_0 LUMO quasi-particle energies for the molecular systems from the GW100 benchmark set for various approximations in the evaluation of the G_0W_0 self-energy relative to the “fully-analytic” approach without employing the RI approximation. Effective core potentials are used for the heavy elements rubidium, silver, xenon, and iodine. Analytic-RI: “Fully-analytic” approach using the RI approximation, AC: AC- G_0W_0 , LT: AC- G_0W_0 in combination with AC-LT ($\varepsilon_{LT} = 10^{-7}$), AC-FC: AC- G_0W_0 in combination with FC, AC-NAF: AC- G_0W_0 in combination with the NAF approximation ($\varepsilon_{NAF} = 10^{\{-6,-4,-2\}}$), AC-FC-LT-NAF: Combining AC- G_0W_0 with FC/LT/NAF ($\varepsilon_{LT} = 10^{-7}$, $\varepsilon_{NAF} = 10^{\{-6,-4,-2\}}$) [def2-TZVP, starting from Hartree–Fock orbitals]. This data is additionally provided as a text file.

	Analytic RI	AC	AC-FC	AC-LT	AC-NAF(6)	AC-NAF(4)	AC-NAF(2)	AC-LT-FC-NAF(6)	AC-LT-FC-NAF(4)	AC-LT-FC-NAF(2)	Analytic
butane	3.131	3.131	3.132	3.131	3.131	3.131	3.136	3.132	3.132	3.140	3.126
carbon tetrabromide	-0.254	-0.254	-0.293	-0.254	-0.254	-0.254	-0.253	-0.293	-0.293	-0.292	-0.256
hydrogen peroxide	3.269	3.269	3.269	3.269	3.269	3.269	3.272	3.269	3.269	3.271	3.269
thymine	0.848	0.848	0.855	0.848	0.848	0.848	0.849	0.855	0.855	0.857	0.848
fluorine	0.814	0.814	0.815	0.814	0.814	0.814	0.814	0.815	0.815	0.816	0.809
toluene	1.845	1.845	1.852	1.845	1.845	1.845	1.847	1.852	1.852	1.854	1.847
ethylbenzene	2.002	2.002	2.008	2.002	2.002	2.002	2.005	2.008	2.008	2.011	2.006
arsenic dimer	-0.361	-0.361	-0.413	-0.361	-0.361	-0.361	-0.360	-0.413	-0.413	-0.412	-0.362
ethane	3.342	3.342	3.342	3.342	3.342	3.342	3.347	3.342	3.342	3.349	3.340
benzene	1.892	1.892	1.899	1.892	1.892	1.892	1.894	1.899	1.899	1.901	1.895
sulfur tetrafluoride	1.035	1.035	1.034	1.035	1.035	1.035	1.036	1.034	1.034	1.035	1.031
tetracarbon	-2.193	-2.193	-2.187	-2.193	-2.193	-2.193	-2.192	-2.187	-2.187	-2.184	-2.193
fluoroborane	1.641	1.641	1.643	1.641	1.641	1.641	1.642	1.643	1.643	1.645	1.641
potassium bromide	-0.382	-0.382	-0.383	-0.382	-0.382	-0.382	-0.372	-0.383	-0.382	-0.374	-0.382
cytosine	1.014	1.014	1.021	1.014	1.014	1.014	1.016	1.021	1.021	1.024	1.015
krypton	10.490	10.490	10.466	10.490	10.490	10.490	10.491	10.466	10.466	10.467	10.489
diborane(6)	1.583	1.583	1.588	1.583	1.583	1.583	1.586	1.588	1.588	1.591	1.583
water	3.126	3.126	3.125	3.126	3.126	3.126	3.126	3.125	3.125	3.126	3.125
formic acid	3.320	3.320	3.320	3.320	3.320	3.320	3.324	3.320	3.320	3.323	3.320
propane	3.184	3.184	3.185	3.184	3.184	3.184	3.189	3.185	3.185	3.192	3.180
phosphine	3.317	3.317	3.320	3.317	3.317	3.317	3.318	3.320	3.320	3.321	3.323
aniline	1.947	1.947	1.954	1.947	1.947	1.947	1.949	1.954	1.954	1.956	1.949
carbon monoxide	1.150	1.150	1.155	1.150	1.150	1.150	1.151	1.155	1.155	1.157	1.151
lithium hydride	0.128	0.128	0.128	0.128	0.128	0.128	0.127	0.128	0.128	0.127	0.125
sodium hexamer	-0.413	-0.413	-0.413	-0.413	-0.413	-0.413	-0.404	-0.413	-0.413	-0.404	-0.421
magnesium fluoride	0.045	0.045	0.045	0.045	0.045	0.045	0.054	0.045	0.045	0.055	0.046
sulfur dioxide	-0.472	-0.472	-0.473	-0.472	-0.472	-0.472	-0.471	-0.473	-0.473	-0.472	-0.473
disilane	2.599	2.599	2.606	2.599	2.599	2.599	2.603	2.606	2.606	2.609	2.595
copper dimer	-0.031	-0.031	-0.031	-0.031	-0.031	-0.031	-0.021	-0.031	-0.031	-0.022	-0.041

ozone	-4.108	-4.108	-4.104	-4.108	-4.108	-4.108	-4.107	-4.104	-4.104	-4.102	-4.108
nitrogen	3.075	3.075	3.080	3.075	3.075	3.075	3.077	3.080	3.080	3.082	3.075
ammonia	3.118	3.118	3.118	3.118	3.118	3.118	3.121	3.118	3.118	3.119	3.115
acetaldehyde	2.181	2.181	2.186	2.181	2.181	2.181	2.183	2.186	2.186	2.188	2.183
hydrogen sulfide	3.117	3.117	3.117	3.117	3.117	3.117	3.119	3.117	3.117	3.118	3.119
sodium chloride	-0.560	-0.560	-0.560	-0.560	-0.560	-0.560	-0.548	-0.560	-0.560	-0.549	-0.560
phosphorus dimer	-0.200	-0.200	-0.207	-0.200	-0.200	-0.200	-0.199	-0.207	-0.207	-0.206	-0.202
ethylene	2.850	2.850	2.855	2.850	2.850	2.850	2.853	2.855	2.855	2.857	2.850
methane	3.664	3.664	3.664	3.664	3.664	3.664	3.667	3.664	3.664	3.670	3.662
cyclopentadiene	1.908	1.908	1.914	1.908	1.908	1.908	1.911	1.914	1.914	1.916	1.908
hydrazine	2.799	2.799	2.800	2.799	2.799	2.799	2.803	2.800	2.800	2.802	2.792
cyclopropane	3.725	3.725	3.725	3.725	3.725	3.725	3.729	3.725	3.725	3.732	3.725
vinyl bromide	2.125	2.125	2.128	2.125	2.125	2.125	2.128	2.128	2.128	2.131	2.126
potassium hydride	-0.018	-0.018	-0.018	-0.018	-0.018	-0.018	-0.002	-0.018	-0.018	-0.002	-0.019
silane	3.375	3.375	3.378	3.375	3.375	3.375	3.378	3.378	3.378	3.382	3.376
guanine	2.116	2.116	2.117	2.116	2.116	2.116	2.122	2.117	2.117	2.121	2.112
neon	21.198	21.198	21.195	21.198	21.198	21.198	21.197	21.195	21.194	21.195	21.199
hydrogen cyanide	3.542	3.542	3.543	3.542	3.542	3.542	3.547	3.543	3.543	3.548	3.541
boron nitride	-3.830	-3.830	-3.823	-3.830	-3.830	-3.830	-3.829	-3.823	-3.823	-3.821	-3.832
urea	2.570	2.570	2.569	2.570	2.570	2.570	2.575	2.569	2.569	2.573	2.565
lithium fluoride	-0.012	-0.012	-0.012	-0.012	-0.012	-0.012	-0.004	-0.012	-0.012	-0.004	-0.012
helium	22.402	22.402	22.402	22.402	22.402	22.402	22.402	22.402	22.402	22.402	22.401
acetylene	3.765	3.765	3.765	3.765	3.765	3.765	3.769	3.765	3.765	3.768	3.763
ethoxy ethane	3.210	3.210	3.211	3.210	3.210	3.210	3.215	3.211	3.211	3.219	3.207
hydrogen fluoride	3.232	3.232	3.232	3.232	3.232	3.232	3.236	3.232	3.232	3.236	3.233
cyclooctatetraene	0.941	0.941	0.948	0.941	0.941	0.941	0.943	0.948	0.948	0.950	0.943
pyridine	1.337	1.337	1.344	1.337	1.337	1.337	1.339	1.344	1.344	1.346	1.339
carbon tetrachloride	1.112	1.112	1.106	1.112	1.112	1.112	1.113	1.106	1.106	1.106	1.112
pentasilane	1.128	1.128	1.137	1.128	1.128	1.128	1.131	1.137	1.137	1.140	1.115
uracil	0.771	0.771	0.778	0.771	0.771	0.771	0.772	0.778	0.778	0.780	0.772
methanol	3.291	3.291	3.291	3.291	3.291	3.291	3.294	3.291	3.291	3.294	3.289
borane	0.708	0.708	0.712	0.708	0.708	0.708	0.710	0.712	0.712	0.714	0.708
carbon tetrafluoride	5.158	5.158	5.157	5.158	5.158	5.158	5.162	5.157	5.157	5.161	5.156
vinyl chloride	2.292	2.292	2.297	2.292	2.292	2.292	2.295	2.297	2.297	2.299	2.293
phenol	1.773	1.773	1.779	1.773	1.773	1.773	1.774	1.779	1.779	1.782	1.775
aluminum fluoride	0.794	0.794	0.815	0.794	0.794	0.794	0.800	0.815	0.815	0.821	0.794
carbon disulfide	0.204	0.204	0.204	0.204	0.204	0.204	0.205	0.204	0.204	0.204	0.204
lithium dimer	0.039	0.039	0.039	0.039	0.039	0.039	0.042	0.039	0.039	0.042	0.028
carbon dioxide	2.980	2.980	2.980	2.980	2.980	2.980	2.985	2.980	2.980	2.983	2.981

phosphorus mononitride	0.354	0.354	0.353	0.354	0.354	0.354	0.355	0.353	0.353	0.354	0.354
argon	14.838	14.838	14.833	14.838	14.838	14.838	14.838	14.833	14.833	14.833	14.837
hydrogen azide	2.081	2.081	2.085	2.081	2.081	2.081	2.083	2.085	2.085	2.087	2.081
hexafluorobenzene	0.910	0.910	0.920	0.910	0.910	0.910	0.911	0.920	0.920	0.922	0.910
vinyl fluoride	2.957	2.957	2.963	2.957	2.957	2.957	2.961	2.963	2.963	2.965	2.958
beryllium monoxide	-2.086	-2.086	-2.086	-2.086	-2.086	-2.086	-2.075	-2.086	-2.086	-2.077	-2.088
carbon oxyulfide	1.784	1.784	1.788	1.784	1.784	1.784	1.785	1.788	1.788	1.789	1.784
formaldehyde	1.902	1.902	1.906	1.902	1.902	1.902	1.904	1.906	1.906	1.908	1.903
ethanol	3.122	3.122	3.123	3.122	3.122	3.122	3.126	3.123	3.123	3.128	3.120
bromine	-0.747	-0.747	-0.818	-0.747	-0.747	-0.747	-0.746	-0.818	-0.818	-0.817	-0.752
germane	3.542	3.542	3.518	3.542	3.542	3.542	3.543	3.518	3.518	3.518	3.542
magnesium chloride	-0.053	-0.053	-0.054	-0.053	-0.053	-0.053	-0.039	-0.054	-0.054	-0.042	-0.051
carbon oxyseleide	1.368	1.368	1.364	1.368	1.368	1.368	1.369	1.364	1.364	1.366	1.368
titanium fluoride	-1.297	-1.297	-1.325	-1.297	-1.297	-1.297	-1.299	-1.325	-1.325	-1.315	-1.304
copper cyanide	-0.732	-0.732	-0.732	-0.732	-0.732	-0.732	-0.724	-0.732	-0.732	-0.723	-0.732
sodium tetramer	-0.461	-0.461	-0.462	-0.461	-0.461	-0.461	-0.452	-0.462	-0.462	-0.448	-0.471
hydrogen chloride	2.928	2.928	2.925	2.927	2.928	2.928	2.930	2.925	2.925	2.926	2.933
arsine	3.235	3.235	3.215	3.235	3.235	3.235	3.235	3.215	3.215	3.215	3.238
magnesium monoxide	-1.519	-1.519	-1.519	-1.519	-1.519	-1.519	-1.506	-1.519	-1.519	-1.506	-1.520
dipotassium	-0.295	-0.295	-0.296	-0.295	-0.295	-0.295	-0.290	-0.296	-0.295	-0.288	-0.310
sodium dimer	-0.206	-0.206	-0.206	-0.206	-0.206	-0.206	-0.198	-0.206	-0.206	-0.199	-0.230
chlorine	0.006	0.006	-0.006	0.006	0.006	0.006	0.007	-0.006	-0.006	-0.006	0.006
adenine	1.444	1.444	1.452	1.444	1.444	1.444	1.446	1.452	1.452	1.455	1.444
gallium monochloride	0.333	0.333	0.309	0.333	0.333	0.333	0.336	0.309	0.309	0.311	0.332
hydrogen	4.367	4.367	4.367	4.367	4.367	4.367	4.367	4.367	4.367	4.367	4.407
dirubidium	-0.336	-0.336	-0.336	-0.336	-0.336	-0.336	-0.324	-0.336	-0.336	-0.324	-0.343
silver dimer	-0.390	-0.390	-0.390	-0.390	-0.390	-0.390	-0.381	-0.390	-0.390	-0.381	-0.391
xenon	7.738	7.738	7.728	7.738	7.738	7.738	7.740	7.728	7.728	7.729	7.738
iodine	-1.331	-1.331	-1.367	-1.331	-1.331	-1.331	-1.330	-1.367	-1.367	-1.365	-1.335
vinyl iodide	1.676	1.676	1.665	1.676	1.676	1.676	1.678	1.665	1.665	1.666	1.674
aluminum iodide	-0.203	-0.203	-0.205	-0.203	-0.203	-0.203	-0.200	-0.205	-0.205	-0.202	-0.203
carbon tetraiodide	-1.403	-1.403	-1.427	-1.403	-1.403	-1.403	-1.402	-1.427	-1.427	-1.427	-1.407

S2 Wall-Clock Timings Water Clusters

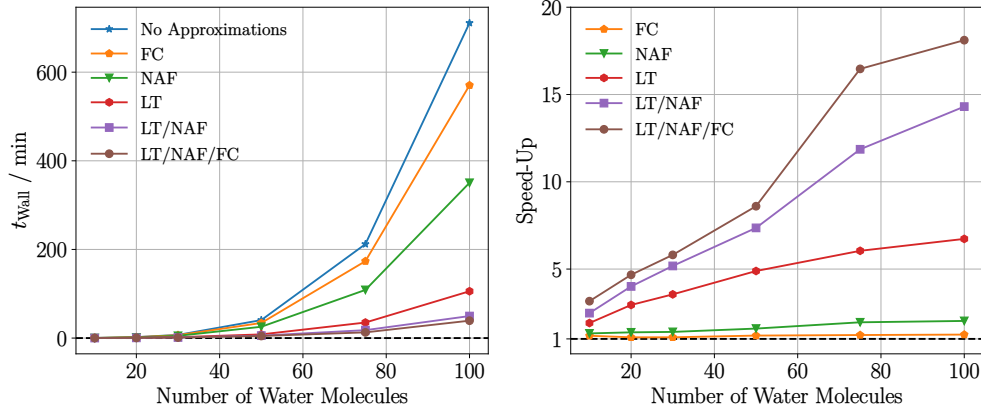


Figure S1: Computational wall-clock timings (left) and resulting speed-ups with respect to no approximations used (right) as a function of the number of water molecules of the AC- G_0W_0 calculations for the water clusters shown in the main text.

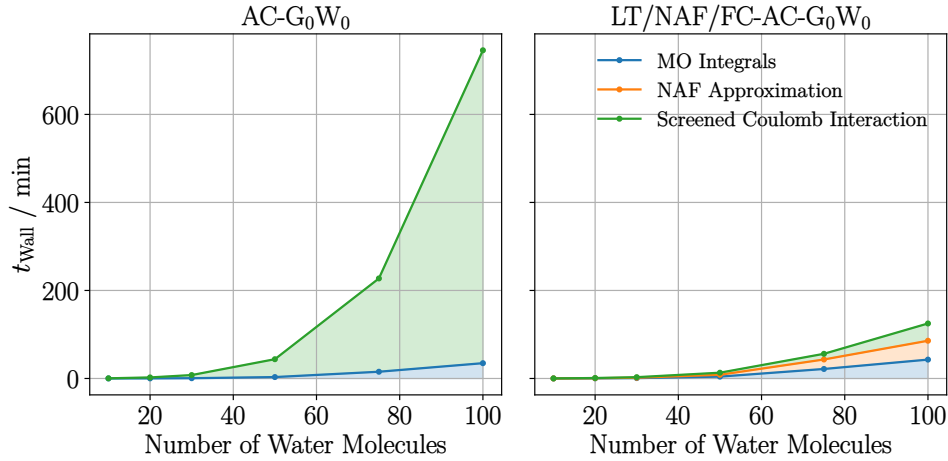


Figure S2: Composition of computational wall-clock timings of the regular AC- G_0W_0 (left) and LT/NAF/FC-AC- G_0W_0 calculations (right) for the water clusters shown in the main text. The graphs are understood as follows: The difference between the green line and the blue one (and not the green line itself) corresponds to the individual timing for the screened Coulomb interaction in the regular AC-GW case (implied with transparent green filling).

Table S3: Computational wall-clock timings (in minutes) for different parts of G_0W_0 calculations for the water cluster containing 100 molecules. Listed are the preceding SCF calculation, the calculation of the screened Coulomb interaction W , the calculation of three-center molecular orbital (MO) integrals, and the natural auxiliary function (NAF) approximation. The calculations further applied a Laplace transformation and the frozen-core approximation. In parentheses are given the speed up with respect to the timing of the same category with half the cores used.

N_{core}	SCF	W	MO Integrals	NAF
6	380	196	271	40
12	203 (1.9)	114 (1.7)	152 (1.8)	23 (1.7)
24	107 (1.9)	70 (1.6)	89 (1.7)	14 (1.6)
48	66 (1.6)	50 (1.4)	62 (1.4)	11 (1.3)
96	43 (1.5)	39 (1.3)	43 (1.4)	11 (1.0)